SLAC-PUB-2761
June 1981
(T/E)

QUARKONIUM SPECTROSCOPY*

Daniel L. Scharre
Stanford Linear Accelerator Center
Stanford University, Stanford, California 94305

ABSTRACT

Recent experimental investigations of heavy quark-antiquark bound state systems are reviewed. Results from SPEAR on charmonium spectroscopy and from DORIS and CESR on bottomonium spectroscopy are presented. The current status of the search for top is also discussed.

(Invited talk presented at the International Conference on Physics in Collision: High Energy ee/ep/pp Interactions, Blacksburg, Virginia, May 28-31, 1981.)

*Work supported by the Department of Energy, contract DE-AC03-76SF00515.

I. INTRODUCTION

The study of quarkonium spectroscopy (i.e., the spectroscopy of nonrelativistic positronium-like bound states formed by heavy quark-antiquark systems) began in 1974 with the simultaneous discovery of the J/ψ(3095) in the reaction[1] $p + Be \to e^+ + e^- + X$ and in e^+e^- annihilations into hadrons.[2] A second narrow resonance was subsequently discovered[3] with a mass approximately 600 MeV greater than the mass of the J/ψ. Although there was some uncertainty as to the origin of these narrow resonances at first, it is now well-established that these and other related states are bound states of a fourth quark, the c or charmed quark.

The next chapter began in 1977 when evidence for the Υ(9460) was observed in proton-nucleus collisions.[4] Better statistics provided evidence for at least one more related particle.[5] The Υ was subsequently observed in e^+e^- annihilations.[6,7] The Υ resonances have been identified as bound states of a fifth quark, the b or bottom quark. The name bottom is based on the assumption that the b quark is the lower (i.e., charge -1/3) member of the third weak isospin doublet of quarks.

It is likely that there is at least one more system of quark-antiquark bound states due to the existence of a sixth quark. This quark, the t or top quark, is expected to be the charge 2/3 partner of the b quark.

In this review, recent results on charmonium and bottomonium spectroscopy are presented. The current status of the search for top is also discussed.

II. CHARMONIUM

Figure 1 shows a level diagram for the charmonium system. The standard spectroscopic notation $n^{2S+1}L_J$ is used where n is the number of radial nodes plus one, S is the total $q+\bar{q}$ spin (0 or 1), L is the orbital angular momentum of the $q\bar{q}$, and J is the total angular momentum of the resonance. Note that not all possible states are shown. In particular, the ^1P and ^3D states are not shown. Solid lines indicate established states or transitions. Experimental identification of established states is shown. Dashed lines indicate unobserved states or transitions.

A. Inclusive Photon Spectra

Of the states shown in Fig. 1, only the J/ψ and the $\psi'(3685)$ can be produced directly in e^+e^- annihilations. The other states are produced via photon transitions from the J/ψ or the ψ'. In Fig. 2, which shows the inclusive photon spectrum from the ψ', nearly all of charmonium spectroscopy is displayed. The data is based on 800,000 ψ' hadronic decays from the Crystal Ball experiment.[8] To clean up the spectrum, photon pairs that can be reconstructed to form a π^0 have been removed. In addition, only photons sufficiently separated from other tracks (both charged and neutral) so that there is no shower overlap have been used.

Peaks corresponding to radiative transitions are identified in the insert. Peaks labeled 1, 2 and 3 result from transitions between the ψ' and the three χ states. The broad enhancement labeled 4 and 5 results from the transitions $\chi(3550) \to \gamma J/\psi$ and $\chi(3510) \to \gamma J/\psi$. The transition

$\chi(3415) \to \gamma J/\psi$ (labeled 6) cannot be seen in this distribution due to its small branching ratio. Finally, the peak at 7 corresponds to the transition $\psi' \to \gamma\eta_c(2980)$.

In contrast to the ψ' inclusive photon spectrum, the J/ψ inclusive photon spectrum (based on approximately 900,000 J/ψ hadronic decays), shown in Fig. 3, is relatively structureless.[8] The arrow at 112 MeV indicates the location of the photon transition from the J/ψ to the η_c. The enhancement near 200 MeV results from minimum-ionizing charged particles which were not tagged as charged by the tracking system.

B. $J/\psi \to \gamma\eta_c$; $\psi' \to \gamma\eta_c$

Figure 4(a) shows the ψ' inclusive photon spectrum in the region of the transition to the η_c. The corresponding distribution from the J/ψ is shown in Fig. 5(a). A simultaneous fit was performed to determine the mass M and width Γ of the η_c from both the J/ψ and ψ' inclusive photon distributions. The two observed signals were fit to a Breit-Wigner line shape convoluted with a Gaussian energy resolution function. Independent quadratic forms were used for the backgrounds. The parameters which were determined from the best fit are $M = 2981 \pm 15$ MeV and $\Gamma = 20^{+16}_{-11}$ MeV. The value of Γ was determined primarily from the J/ψ inclusive spectrum and no additional uncertainty due to the choice of the functional form which was used for the background was included in the error. Figures 4(b) and 5(b) show the photon energy distributions after background subtraction. The curves represent the results of the best fit to the data.

Based on the results of this fit, the branching ratio for the process

$$\psi' \to \gamma\eta_c \qquad (1)$$

is measured to be[8] $B(\psi' \to \gamma\eta_c) = 0.43 \pm 0.08 \pm 0.18\%$, where the first error is statistical and the second is systematic. The branching ratio for the process

$$J/\psi \to \gamma\eta_c \qquad (2)$$

is not reliably known due to uncertainties in the shape of the background. Preliminary estimates of the branching ratio[3] are between 0.4 and 4%.

The exclusive process

$$J/\psi \to \gamma\eta_c \ , \ \eta_c \to \eta\pi^+\pi^- \qquad (3)$$

has been observed directly by the Crystal Ball.[8] Figure 6 shows the photon energy distribution for events which satisfy constrained fits to the hypothesis

$$J/\psi \to \gamma\eta\pi^+\pi^- \ , \ \eta \to \gamma\gamma \quad .$$

A clear signal is seen which corresponds to a mass for the η_c of $M = 2974 \pm 9$ MeV. The width of the observed signal is narrow and consistent with the expected energy resolution. When these results are combined with the previous results from the inclusive photon spectra, the best values of the η_c resonance parameters are determed to be $M = 2978 \pm 9$ MeV and $\Gamma < 20$ MeV (90% confidence level). The branching ratio product for (3) is measured to be $B(J/\psi \to \gamma\eta_c) \times B(\eta_c \to \pi^+\pi^-\eta) = (3.1 \pm 1.1 \pm 1.5) \times 10^{-4}$. Depending on the branching ratio for (2), this leads to a branching ratio for $\eta_c \to \pi^+\pi^-\eta$ on the order of 1-10%.

The Mark II experiment has observed the η_c in transitions from the ψ' by analysis of final hadronic states which satisfy fits to the following hypotheses[10]

$$\psi' \to \gamma p\bar{p}$$
$$\psi' \to \gamma\pi^+\pi^-\pi^+\pi^-$$
$$\psi' \to \gamma\pi^+\pi^-K^+K^-$$
$$\psi' \to \gamma\pi^+\pi^-p\bar{p}$$
$$\psi' \to \gamma K^\pm\pi^\mp K_S \ , \quad K_S \to \pi^+\pi^-$$

The analysis was based on a study of one million ψ' decays. The combined fitted hadronic mass distribution for these five processes is shown in Fig. 7. A background subtraction has been made for contamination due to events with single π^0's rather than single γ's. A peak at the mass of the η_c is observed. A fit to the distribution gives $M = 2980 \pm 8$ MeV and $\Gamma < 40$ MeV (90% confidence level), in agreement with the Crystal Ball results. The branching ratio products for

$$\psi' \to \gamma\eta_c, \quad \eta_c \to \text{hadrons}$$

are given in Table I. From the measured inclusive branching ratio for (1) from the Crystal Ball, the η_c hadronic branching ratios can be extracted. They are also given in Table I.

The experimental parameters which have been measured for the η_c are not in gross disagreement with theoretical expectations. Estimates[11,12] for the ground state hyperfine splitting (i.e., the $J/\psi - \eta_c$ mass difference) are the order of 100 MeV. This is to be compared with the experimental value of approximately 120 MeV. Estimates[13] for the total

width of the η_c (based on a Coulomb + linear potential) are on the order of 5 MeV. The present experimental upper limits are still considerably larger than this prediction. No detailed estimates for branching ratios of hadronic states from the η_c have been published. However, estimates of branching ratios for radiative transitions to the η_c have been made. The theoretical expectations[14] according to a Coulomb + linear potential are $B(J/\psi \to \gamma\eta_c) \approx 3\%$ and $B(\psi' \to \gamma\eta_c) \approx 0.5\%$. The ψ' branching ratio prediction is in excellent agreement with the experimental measurement. The predicted J/ψ branching ratio is within the range of values covered by experiment.

C. $\psi' \to \gamma\chi$, $\chi \to \gamma J/\psi$

As shown in the level diagram in Fig. 1, all three χ states are produced in the double-cascade process

$$\psi' \to \gamma\gamma J/\psi \quad . \tag{4}$$

The hadronic transitions

$$\psi' \to \eta J/\psi \tag{5}$$

and

$$\psi' \to \pi^0 J/\psi \tag{6}$$

can also be observed in this process. Both the Mark II[15] and the Crystal Ball[16] have new results from an analysis of (4) based on substantially greater statistics than were available to previous experiments. In both experiments, the J/ψ is identified by means of its decay into e^+e^- or $\mu^+\mu^-$.

Figure 8 shows the low mass vs. the high-mass $\gamma J/\psi$ invariant mass combinations from the Mark II for events which satisfy constrained fits

to (4). Events consistent with (5) have been eliminated. Vertical bands due to the χ_1 and χ_2 produced in the double-cascade process

$$\psi' \to \gamma\chi, \quad \chi \to \gamma J/\psi \tag{7}$$

are observed. [For simplicity of notation, it will be assumed that the $\chi(3415)$ is spin 0, the $\chi(3510)$ is spin 1, and the $\chi(3550)$ is spin 2. These are the theoretically preferred assignments. These states will be referred to as χ_0, χ_1 and χ_2, respectively. A review of the current experimental situation with regard to the spins will be discussed later.] Peaks due to these two states are clearly seen in the high-mass projection. Kinematic reflections of these peaks arising from combinations of the J/ψ with the initially emitted photon dominate the low-mass projection. The curves in Fig. 8 represent the results of a fit to the χ_1 and χ_2 peaks plus background.

Figure 9 shows a similar scatter plot from the Crystal Ball. Again, bands due to the χ_1 and χ_2 are seen. In addition there is a band along the lower edge of the allowed region of phase space due to (5). The data can be plotted in a different manner to make the processes involved more apparent. This is shown in the Dalitz plot in Fig. 10. The outer curve shows the phase space boundary. Cuts due to the detector (e.g., shower overlap cuts) reduce the phase space as shown by the inner curve. Plotted in this manner, the correct $\gamma J/\psi$ mass combinations (in the right half of the plot) appear as vertical bands. The wrong $\gamma J/\psi$ mass combinations deviate from the vertical. Horizontal bands due to (5) and (6) can also be seen.

The $\gamma J/\psi$ invariant mass projection (high-mass combination only) from the Crystal Ball is shown in Fig. 11. Events consistent with (5) and (6) have been eliminated. In addition to clean peaks at the masses of the χ_1 and the χ_2, there is an excess of events at the mass of the χ_0. A possible background to (4) is the process

$$\psi' \to \pi^0\pi^0 J/\psi \quad , \tag{8}$$

where a reasonable fit to (4) can be made with observation of only two of the photons from the π^0 decays. Although the process (8) has a large branching ratio, the contamination due to this process is quite small as shown by the dotted curve in Fig. 11 which represents one hundred times the expected background from (8). This background does not account for the observed χ_0 signal, thus it is believed to be real. The solid curve in Fig. 11 shows a fit to the data including peaks at the χ_1 and χ_2.

Evidence for the χ_0 is marginal in this double-cascade process. The fact that it is a well-established state is shown in Fig. 12. The exclusive processes $\psi' \to \gamma +$ hadrons have been analyzed in detail by the Mark II.[17] The hadronic invariant mass distributions for events which satisfy constrained fits to the processes $\psi' \to \gamma 2\pi^+ 2\pi^-$ and $\psi' \to \gamma 3\pi^+ 3\pi^-$ are shown in Figs. 12(a) and (b). Clear peaks at the masses of all three χ states are seen.

The new mass determinations of the χ states are more accurate than previously measured values due to the large event samples available from the Mark II and Crystal Ball experiments. The χ_1 and χ_2 masses have been determined from fits to (4). The χ_0 mass has been determined

from fits to hadronic decays of the χ_0, such as those shown in Fig. 12. These results are summarized in Table II.

The branching ratio products $B(\psi' \to \gamma\chi) \times B(\chi \to \gamma J/\psi)$ were determined from fits to the invariant mass distributions shown in Figs. 8 and 11. The results are given in Table III along with previous measurements from other experiments. If the average measured branching ratio products are divided by the measured $\psi' \to \gamma\chi$ branching ratios [$B(\psi' \to \gamma\chi) = 7 \pm 2\%$ for all three χ states[21]], the $\chi \to \gamma J/\psi$ branching ratios can be determined. They are given in Table IV. The small $\chi_0 \to \gamma J/\psi$ branching ratio accounts for the difficulty in observing the χ_0 in the double cascade decay (7).

In terms of theoretical comparisons, the radiative widths of the states are more relevant than the branching ratios. To calculate these partial widths, it is necessary to know the total widths of the χ states. A preliminary measurement of the total width of the χ_0 has been made from a fit to the inclusive photon spectrum at the ψ' (see Fig. 2). The result is $\Gamma(\chi_0) = 10 \pm 3$ MeV.[22,23] The total widths of the χ_1 and χ_2 have been measured by fitting the peaks in Fig. 11. This data is shown again in Fig. 13 as a function of photon energy rather than invariant mass. The data were fitted to two Breit-Wigner peaks convoluted with the NaI energy resolution function. The best fit is shown by the solid curve. The χ_1 peak ($E_\gamma \simeq 170$ MeV) has a width consistent with the energy resolution with 90% confidence level upper limit $\Gamma < 2.6$ MeV. The χ_2 peak ($E_\gamma \simeq 130$ MeV) is best fit with a natural width of $\Gamma = 4 \pm 1$ MeV. The error is statistical only. If one forces the width to be 0, the best fit is shown by the dashed curve. It is clear that the nonzero value for the width is being forced by the excess of events between the

two peaks. Thus, if there were an unknown background which populated this region, the fitted width might be unnaturally high. Therefore, if systematic uncertainties are considered, the measured value of the width of the χ_2 should be taken as an upper limit.

Table V summarizes the χ total width measurements and the χ radiative width measurements which were determined from the products of the χ total widths and radiative branching ratios. Also shown are the theoretical expectations as determined from several theoretical models.[14,24,25] Considering the uncertainties in both the experimental numbers and the theoretical predictions, it is difficult to claim that the numbers are not in agreement.

Based on gluon-counting assumptions (i.e., hadronic decays of the χ_0 and the χ_2 proceed via two gluons in lowest order), the ratio of the χ_2 and χ_0 hadronic widths is[13]

$$\frac{\Gamma(\chi_2 \to \text{hadrons})}{\Gamma(\chi_0 \to \text{hadrons})} = \frac{4}{15} = 0.27 \quad .$$

From the difference between the experimentally determined total widths and radiative widths, one determines

$$\frac{\Gamma(\chi_2 \to \text{hadrons})}{\Gamma(\chi_0 \to \text{hadrons})} \leq 0.34 \pm 0.13 \quad .$$

The χ_1 is expected to have a hadronic width smaller than either the χ_0 or the χ_2. This is consistent with experimental measurements.

Previous experimental results on the spins of the χ states are in agreement with the theoretical assignments $J^P = 0^+$, 1^+ and 2^+ for the χ_0, χ_1 and χ_2, respectively. On the other hand, the experimental

assignments could not be made unambiguously. A recent Crystal Ball spin analysis of the process

$$\psi' \to \gamma\chi, \ \chi \to \gamma J/\psi, \ J/\psi \to \ell^+\ell^- \qquad (9)$$

provides unambiguous assignments for the χ_2 and χ_1 as discussed below.

The χ_2 has previously been observed to decay into $\pi^+\pi^-$ and K^+K^-.[26] Since both decay products are pseudoscalar, the χ_2 must have $J^{PC} = 0^{++}$, 1^{--} or 2^{++}. (Higher spin states are not considered.) Since the χ_2 is produced in a radiative transition from the ψ' (as are the other two states), the C-parity must be even, thus eliminating $J^{PC} = 1^{--}$. The $\cos\theta_\gamma$ distribution, where θ_γ is the angle between the photon produced in the $\psi' \to \gamma\chi$ transition and the beam axis, is shown in Fig. 14(a). This distribution alone is not sufficient to separate the spin 2 (solid curve) and spin 0 (dashed curve) hypotheses. A maximum likelihood fit to the data involving the five polar and azimuthal angles entering the full decay process (9) has been made. The results, given in Table VI, clearly favor the spin 2 hypothesis.

Nonobservation of the decay of the χ_1 into pairs of pseudoscalars suggests an unnatural spin-parity assignment $J^{PC} = 0^{-+}$, 1^{++}, 2^{-+}. Furthermore, the χ_1 is observed to decay into $\pi^\pm K^\mp K_S^0$,[15] thus eliminating the possibility of a $J^P = 0^+$ assignment. The $\cos\theta_\gamma$ distribution is shown in Fig. 14(b). The spin 1 hypothesis (solid curve) provides a better fit than either spin 0 (dashed curve) or spin 2 (the expected distribution is similar to the spin 0 distribution). The results of the full maximum likelihood fit, also given in Table VI, favor the spin 1 hypothesis.

The X_0 has $J^{PC} = 0^{++}$ or 2^{++} since it has also been observed to decay into $\pi^+\pi^-$ and K^+K^-. The $\cos\theta_\gamma$ distribution, as shown in Fig. 14(c), is consistent with spin 0. Due to the limited statistics available, it is impossible to do a maximum likelihood fit to the data. However, if we consider the evidence from hadronic decays of the X_0 which show the angular distribution to be consistent with $1 + \cos^2\theta_\gamma$,[26] the likely assignment for this state is $J^{PC} = 0^{++}$.

D. $\psi' \to \eta J/\psi$

Figures 15 and 16(a) show the $\gamma\gamma$ invariant mass distributions for (4) from the Mark II[15] and the Crystal Ball,[27] respectively. A clear η peak from (5) is observed in both distributions. In addition to the background from (7), there is also background from (8) where only two of the four produced photons are observed. The feeddown from this process has been estimated by both the Mark II and Crystal Ball experiments and is shown by the curves in Figs. 15 and 16(a) situated near the upper end of the $\gamma\gamma$ mass spectrum. [For the Crystal Ball, the curve represents ten times the estimated background from (8).] Clearly, it is important to understand this background if reliable branching ratios for (5) are to be extracted.

Branching ratios determined from these distributions are given in Table VII along with previously measured branching ratios. The new measurements are somewhat lower than older measurements. This may be due to a more careful analysis of the background from (8).

The decay $\psi' \to \eta J/\psi$ is peculiar in that the branching ratio is much larger than would be naively expected. If one compares this branching ratio with the $\psi' \to \pi\pi J/\psi$ branching ratio,[21] one gets

$B(\psi' \to \eta J/\psi)/B(\psi' \to \pi\pi J/\psi) \approx 6\%$. This level of suppression relative to the $\pi\pi$ transition can be explained by phase space alone. (The decay must be p-wave and hence a factor k^3 enters into the width.) In addition, there is the fact that only an SU(3) singlet state can couple between the two charmonium states. Since the η is mostly octet, this contributes an additional suppression of at least a factor of ten. There are two possible solutions to this problem. One can assume that there is a $c\bar{c}$ admixture in the η so that it can couple directly to the $\psi' - J/\psi$ system. Such models[30,31] are capable of explaining not only the large rate for $\psi' \to \eta J/\psi$, but also the rates for $J/\psi \to \gamma\eta$ and $J/\psi \to \gamma\eta'$. Alternatively, one can assume that there is a large 2-gluon component to the η.[32] Thus, the OZI suppression is overcome. This model is also successful in explaining the $J/\psi \to \gamma\eta$ and $J/\psi \to \gamma\eta'$ rates.

E. $\psi' \to \pi^0 J/\psi$

Figure 16(b) shows the $\gamma\gamma$ invariant mass distribution for (4) from the Crystal Ball after elimination of events consistent with the processes (5) and (7). A clean signal at the mass of the π^0 is observed. The branching ratio is measured to be[27] $B(\psi' \to \pi^0 J/\psi) = 0.09 \pm 0.02\%$. The Mark II has also observed this transition[15] and finds $B(\psi' \to \pi^0 J/\psi) = 0.15 \pm 0.06\%$.

This transition is of particular interest as it violates isospin. There is a nonresonant, electromagnetic process

$$e^+e^- \to \pi^0 J/\psi \qquad (10)$$

which does not violate isospin, but the contribution from this process at the ψ' is expected to be small. In fact, an analysis of process (10)

by the Crystal Ball at 3.77 GeV center-of-mass energy leads to an upper limit of < 0.01% (90% confidence level) for this process at the ψ'. Several papers have made theoretical predictions for the $\psi' \to \pi^0 J/\psi$ branching ratio.[33-36] The calculations involve the mixing of SU(2) and SU(3) eigenstates to form the physical π^0, η and η' states and also consider the effects of SU(2) and SU(3) symmetry breaking in the decay amplitudes. Recent calculations[37-39] lead to branching ratio values in the neighborhood of 0.1%, compatible with experimental results.

F. $\psi' \to \pi\pi J/\psi$

One final transition linking the ψ' and J/ψ has been observed, that is $\psi' \to \pi\pi J/\psi$. This is a well-established transition with $B(\psi' \to \pi\pi J/\psi) = 50 \pm 4\%$.[21] Fig. 17 shows the $\pi\pi$ invariant mass squared for the processes $\psi' \to \pi^+\pi^- J/\psi$ (from the Mark II[17]) and $\psi' \to \pi^0\pi^0 J/\psi$ from the Crystal Ball[27]). The two distributions are consistent in shape (the normalization is arbitrary) and clearly inconsistent with the phase space distribution (the dashed curve). This will be discussed later when a comparison to Υ' data can be made.

III. BOTTOMONIUM

Figure 18 shows a level diagram for some of the more important bottomonium states and the transitions between them. The most significant difference between this diagram and the charmonium level diagram shown in Fig. 1 is the scarcity of established states and transitions for the bottomonium system as compared to the charmonium system. In fact, only those states which are formed directly in e^+e^- annihilations, the $\Upsilon(9460)$, $\Upsilon(10020)$, $\Upsilon''(10350)$ and $\Upsilon'''(10570)$, have been observed.

Only one transition, $\Upsilon' \to \pi^+\pi^-\Upsilon$ has been observed. This is not too surprising, however, when one considers that data at the charmonium resonances can be accumulated at a rate approximately two orders of magnitude higher than the corresponding rate for a given bottomonium resonance.

A. Bottomonium Masses and Widths

Figures 19 and 20 show the hadronic cross section as a function of center-of-mass energy W throughout the Υ resonance region as measured by the CLEO[40,41] and CUSB[42,43] experiments at CESR. In Fig. 19, only the three lower Υ states, the Υ, Υ' and Υ'', are shown. In Fig. 20, the Υ'' and Υ''' states are shown. Note that the CUSB data shown in Fig. 20(b) has a thrust cut ($T \leq 0.85$) applied to the data to enhance the $b\bar{b}$ decays.

A summary of the Υ resonance masses as measured by the CESR experiments and the earlier DORIS experiments is given in Table VIII. The first error in all cases is statistical and the second is systematic. (If only one error is given, it is the combined statistical and systematic error). In the case of M_Υ, the systematic errors are due to the uncertainties in the absolute energy calibrations of the two machines. For DORIS, the uncertainty is 0.1% and for CESR, the uncertainty is 0.3%. Note that the difference between the DORIS and CESR determinations of M_Υ of approximately 30 MeV is consistent with the uncertainty in the energy calibration.

Also of primary importance in the understanding of the bottomonium system are the leptonic widths of the resonances as they are proportional to the squares of the wave functions at the origin. To lowest order

in QCD[11,44,45]

$$\Gamma_{ee} = \frac{4}{9}\,\frac{\alpha^2}{M^2}\,|\psi(0)|^2 \quad , \tag{11}$$

where $\psi(0)$ is the wave function at the origin and M is the mass of the resonance. (The charge of the b quark is assumed to be -1/3, a question which will be addressed shortly.) Experimentally, the leptonic width can be determined from the integrated hadronic cross section $\sigma_{had}(M)$ of the resonance

$$\tilde{\Gamma}_{ee} = \frac{\Gamma_{ee}\Gamma_{had}}{\Gamma_{tot}} = \frac{M^2}{6\pi^2}\int \sigma_{had}(M)\,dM \quad , \tag{12}$$

where $\tilde{\Gamma}_{ee}$ is the reduced leptonic width, Γ_{had} is the hadronic width, and Γ_{tot} is the total width.

Measurements of the reduced leptonic widths for the four T resonances are given in Table IX. First, concentrate on the $\tilde{\Gamma}_{ee}(T)$ column. The average reduced leptonic width is $\bar{\tilde{\Gamma}}_{ee}(T) = 1.08 \pm 0.06$ keV. To first order one can assume that most of the width of the T is into hadronic decays, and hence from (12), the true leptonic width is approximately equal to the reduced leptonic width. To next order, the total width can be broken down as follows

$$\Gamma_{tot} = \Gamma_{had} + \Gamma_{ee} + \Gamma_{\mu\mu} + \Gamma_{\tau\tau} \quad .$$

Assuming e-μ-τ universality,

$$\Gamma_{tot} = \Gamma_{had} + 3\Gamma_{ee} \tag{13}$$

or

$$\Gamma_{had}/\Gamma_{tot} = 1 - 3B_{ee} \quad , \tag{14}$$

where B_{ee} is the leptonic branching ratio. From Eqs. (12) and (14), the true leptonic width can be expressed in terms of the reduced leptonic width and the leptonic branching ratio

$$\Gamma_{ee} = \tilde{\Gamma}_{ee} / (1 - 3B_{ee}) \quad . \tag{15}$$

Note that this is valid for any resonance for which (13) applies. [Depending on the experiment, there may be a small correction to (15) due to the fact that some of the $\tau^+\tau^-$ decays of the T may be found in the hadronic data sample. This correction is neglected in all calculations and is small compared to other errors.]

The leptonic branching ratio of the T has been measured by determining the rate of e^+e^- or $\mu^+\mu^-$ production at the T compared to hadronic production (after subtraction of the nonresonant background contribution). The measured values are given in Table X. The average of the measurements (assuming e-μ universality) is $B_{ee}(T) = 3.4 \pm 0.7\%$. This is to be compared with $B_{ee}(J/\psi) = 7 \pm 1\%$ at the J/ψ. From Eq. (15) and the measured value for $\tilde{\Gamma}_{ee}(T)$, the true leptonic width can be calculated, $\Gamma_{ee}(T) = 1.20 \pm 0.07$ keV. From these two measurements, one can also calculate the total width of the T, $\Gamma_{tot}(T) = \Gamma_{ee}(T)/B_{ee}(T) = 35.3^{+9.4}_{-6.4}$ keV. This is to be compared with $\Gamma_{tot}(J/\psi) = 63 \pm 9$ keV.

The hadronic decays of the T are assumed to proceed via an intermediate state consisting of three color-octet gluons in lowest order in QCD. The partial width for this process is predicted to be[11,45]

$$\Gamma_{3g} = \frac{40}{81} \frac{(\pi^2 - 9)}{\pi} \frac{\alpha_s^3}{\mu^2} |\psi(0)|^2 \quad , \tag{16}$$

where α_s is the strong-coupling constant. As in the case of the leptonic width given in (11), the 3-gluon partial width is proportional to the square of the wave function at the origin. Dividing (16) by (11), we eliminate this factor

$$\frac{\Gamma_{3g}}{\Gamma_{ee}} = \frac{10}{9} \frac{(\pi^2 - 9)}{\pi} \frac{\alpha_s^3}{\alpha^2} \quad . \tag{17}$$

With an experimental measurement of Γ_{3g}, it is possible to determine α_s. The total width given in Eq. (13) can be reexpressed as

$$\Gamma_{tot} = \Gamma_{3g} + \Gamma_{em} + 3\Gamma_{ee} \quad , \tag{18}$$

where Γ_{em} is the partial width for second-order electromagnetic decays of the T into hadrons. In this approimation, all direct hadronic decays of the T are identified with the 3-gluon decay. In addition, radiative terms (e.g., γgg decays) are neglected. Since Γ_{em} is the result of nonresonant hadron production, $\Gamma_{em} = R\Gamma_{ee}$, where $R = \sigma_{had}/\sigma_{\mu\mu}$ off-resonance near the T. From experiment, $R \approx 3.7$. Thus, from (18),

$$\Gamma_{tot} = \Gamma_{3g} + 6.7\Gamma_{ee}$$

or

$$\frac{\Gamma_{3g}}{\Gamma_{ee}} = B_{ee}^{-1} - 6.7 \tag{19}$$

Equating (17) and (19) and using measured values for $\Gamma_{ee}(T)$ and $B_{ee}(T)$, one determines $\alpha_s(T) = 0.16 \pm 0.02$. This is to be compared with $\alpha_s(J/\psi) = 0.19 \pm 0.02$, calculated in the same manner. Since higher-order QCD corrections have not been included, the actual values of α_s which are determined in this way may not be meaningful. However, the

small variation that is observed between the J/ψ and the T is consistent with expectations from QCD for a running coupling constant.

Returning now to the data in Table IX, the ratios of the reduced leptonic widths of the T', T" and T'" to the leptonic width of the T are given. These ratios can be determined more accurately from the experimental data than can the reduced leptonic widths themselves as systematic uncertainties tend to cancel in the ratios. Also, theoretical estimates of the ratios are probably subject to less uncertainty than the widths themselves. Finally, note that the denominator in the ratios is $\Gamma_{ee}(T)$ whereas the quantity directly accessible to experiment has $\tilde{\Gamma}_{ee}(T)$ in the denominator. Ratios given in this Table have been corrected by the factor $\tilde{\Gamma}_{ee}(T)/\Gamma_{ee}(T)$ as determined from the average value of B_{ee} (see Table X).

In contrast to the situation for the T, there have been no direct measurements of the leptonic branching ratios of the other T resonances. For the T', the LENA group has set an upper limit $B_{ee}(T') < 3.8\%$ (90% confidence level).[49] However, based on some measurements to be discussed later, a model-dependant calculation permits the determination of the leptonic branching ratio of the T', $B_{ee}(T') = 2.0 \pm 0.4\%$. From the data in Table IX and Eq. (15), $\Gamma_{ee}(T') = 0.57 \pm 0.04$ keV.

B. Potential Model Comparisons

A number of theorists have attempted to understand the ψ and T family mass differences and leptonic widths based on a variety of flavor and spin independent potentials. The standard treatment is to consider the heavy quark-antiquark binding in the nonrelativistic approximation, much the same way as positronium.[11] The potentials vary from arbitrary

functional forms, empirically fit to the data, to potentials inspired by QCD.

The similarity of the $c\bar{c}$ and $b\bar{b}$ level spacings suggests that the potential is approximately logarithmic where the wave function of the bound state is large. The most trivial example of such a potential

$$V(r) = A \ln r \quad ,$$

where r is the radius, has been proposed by Quigg and Rosner.[57] An equally ad hoc power law potential

$$V(r) = A + Br^{\nu}$$

has been proposed by Martin.[58] A good fit to the data is achieved with $\nu \approx 0.1$

From QCD arguments, one-gluon exchange, leading to a Coulombic 1/r dependence, is expected to dominate the form of the potential at small distances. Long-range confinement can be attained by requiring the potential to be linear at large distances. The simplest such potential, originally proposed by the Cornell Group,[14] is the sum of a Coulomb and linear term

$$V(r) = -\frac{4}{3}\frac{\alpha_s}{r} + \frac{r}{a^2} \quad .$$

Bhanot and Rudaz[59] have proposed a piecewise combination of a Coulomb, logarithmic and linear potential

$$V(r) = -\frac{4}{3}\frac{\alpha_s}{r} \qquad r \leq r_1$$

$$= b \ln \frac{r}{r_0} \qquad r_1 \leq r \leq r_2$$

$$= \frac{r}{a^2} \qquad r \geq r_2 \quad .$$

where $r_1 = 0.12$ fm and $r_2 = 0.87$ fm. The potential and its first derivative are required to be continuous at r_1 and r_2.

Richardson[60] has attempted to directly incorporate first-order QCD in the potential. In momentum space,

$$V(q^2) = -\frac{4}{3}\,\frac{12\pi}{33-2n_f}\,\frac{1}{q^2}\,\frac{1}{\ln\left(1+\frac{q^2}{\Lambda^2}\right)} \quad ,$$

where n_f is the number of quark flavors and Λ is a scale parameter. The Fourier transform V(r) matches the single gluon exchange form at small r and joins smoothly to a linear behavior at large r. Richardson's potential has since been modified to take second-order QCD into account explicitly.[61]

In general, the parameters of these models are fixed using charmonium and/or bottomonium masses and leptonic widths as inputs. Figure 21 shows each of these five potentials as a function of r. Also shown are the mean values of the radius for the ^3S ψ and Υ resonances. For the range of r covered by these resonances, the potentials are seen to be fairly similar. Table XI gives a comparison of experimental and theoretical masses and leptonic widths for the ψ and Υ systems. Values in parenthesis are inputs to the models. It is clear that all of the models agree reasonably well with the data. This is to be expected since the potentials are all fairly similar in the intermediate region of r which is most relevant. The major disagreement is for the mass of the $\Upsilon(4S)$ state, but as it is above threshold and can couple to other channels, the bound state models are not expected to provide good predictions for this state.

The data now available is not sufficient to differentiate among the various models. Hopefully, information from the toponium system, or from the heavy quark flavor dependence of the fine structure, will help.

C. b Threshold

The T''' state shown in Fig. 20 is clearly wider than the T'' state. Table XII gives the measured widths of all four T resonances assuming Gaussian resolution functions. The data is from CLEO.[50] The widths of the first three resonances are consistent with the expected CESR machine resolution. The T''' has a width approximately twice the expected resolution. The natural width can be unfolded from the measured distribution. CLEO finds $\Gamma = 9.6 \pm 2.3$ MeV. A similar analysis by the CUSB experiment measures $\Gamma = 12.6 \pm 6.0$ MeV. The fact that the width of this state is more than two orders of magnitude larger than the width of the T indicates that strong decays can proceed directly from the T''' without OZI suppression. That is, pairs of particles with b quantum number ±1 are being produced in the decay of the T'''.

The number of bound states below threshold can be obtained semi-classically from the Bohr-Sommerfeld quantization condition

$$n = \frac{1}{4} + b\, m_Q^{\frac{1}{2}} \quad , \qquad (2^{\wedge})$$

where m_Q is the mass of the heavy quark and b is an undetermined constant. Quigg and Rosner[62] calculated b from the known charmonium threshold energy and predicted n = 3 for the bottomonium system (before the observation of the T'' and T'''). Previous analyses[63] have also predicted a similar increase in the number of bound states as the quark mass increases. Figure 22 shows the energy of the heavy quark continuum

threshold as a function of m_Q/m_c relative to the ^3S onium bound state levels. The actual level spacings are based on a logarithmic potential and hence are independent of quark mass. However, Eq. (20) is more general and applies to a wide range of potential models.

D. Charge of the b Quark

Based on the pattern observed for the u, d, s and c quarks, it is logical to consider the b quark as the bottom member of a third left-handed, weak isospin doublet of quarks. Thus, the charge of the b quark is expected to be -1/3. It is very important to verify this assignment.

Based on very general assumptions about the nature of the $Q\bar{Q}$ potential, theoretical lower limits which depend on the charge e_Q of the heavy quark can be established.[64] As applied to the T system, the limits are as follows

$$\frac{\Gamma_{ee}(T)}{e_b^2} > 2.6 \text{ keV}$$

$$\frac{\Gamma_{ee}(T')}{e_b^2} > 1.4 \text{ keV} \quad .$$

Figure 23 shows the allowed regions for charge assignments of 2/3 and -1/3 as functions of $\Gamma_{ee}(T)$ and $\Gamma_{ee}(T')$. The experimental result (based on numbers presented here) lies just outside the allowed region for a charge 2/3 quark and well within the allowed region for a charge -1/3 quark.

Figure 24 shows Γ_{ee}/e_Q^2 as a function of mass for the well-established vector meson resonances. For the T resonances, $e_b = -1/3$ was assumed. It is observed that Γ_{ee}/e_Q^2 is approximately constant for

the nonradially excited resonances. Likewise, Γ_{ee}/e_Q^2 for the ψ' and T' are approximately equal. This provides additional, although somewhat circumstantial, evidence for the charge -1/3 assignment of the b quark.

The most convincing evidence for this charge assignment is obtained from the hadronic cross section measurements in the T resonance region. According to the naive parton model, and to leading order in QCD, the ratio of the hadronic cross section σ_{had} to the μ-pair point cross section is

$$R = \frac{\sigma_{had}}{\sigma_{\mu\mu}} \approx 3 \sum_{Q=1}^{n_f} e_Q^2 \quad ,$$

where n_f is the number of quark flavors. Thus, as threshold is crossed for production of a new flavor, an increase in the hadronic cross section

$$\Delta R \approx 3e_Q^2 \qquad (21)$$

is expected. If the b is a charge 2/3 quark, an increase of $\Delta R = 4/3$ is expected and if it is a charge -1/3 quark, an increase of only $\Delta R = 1/3$ is expected.

Figure 25 shows R in the region of the T'''' as measured by CUSB.[65] Fits to the measured cross section below and above the resonance give the following results

$$R = 3.73 \pm 0.08 \pm 0.37 \quad , \quad W < M_{T''''}$$

$$R = 4.12 \pm 0.06 \pm 0.37 \quad , \quad W > M_{T''''} \quad ,$$

where the first error is statistical and the second is systematic. The change in R as threshold is crossed is $R = 0.39 \pm 0.10 \pm 0.06$, consistent with a charge -1/3 assignment for the b quark.

One can also invoke duality arguments which imply that the "smeared" cross section due to the narrow bound state resonances should contribute a similar increase in R below threshold. This increase can be expressed in terms of the integrated cross sections[66]

$$\Delta R = \frac{\frac{1}{\Delta M}\int \sigma_{had}(M)\, dM}{\sigma_{\mu\mu}}$$

or in terms of the leptonic widths of the resonances

$$R = \frac{9\pi}{2\alpha^2}\frac{\Gamma_{ee}}{\Delta M} \quad .$$

For a given resonance, I take ΔM to be the average of the mass difference between the resonance and the next lower resonance and the mass difference between the resonance and the next higher resonance. For example, for the T'

$$\Delta M = \frac{1}{2}\left[\left(M_{T'} - M_{T}\right) + \left(M_{T''} - M_{T'}\right)\right] \quad .$$

The resulting contributions to R are as follows

$$\Delta R(T') = 0.34 \pm 0.03$$

$$\Delta R(T'') = 0.33 \pm 0.04 \quad .$$

These results support the -1/3 charge assignment and disagree with the 2/3 charge assignment.

E. $T' \to \pi^+\pi^- T$

The observation of the transition

$$T' \to \pi^+\pi^- T \qquad (22)$$

is important as it establishes that the T and T' are related states and their proximity to each other in mass is not purely coincidental. The $\pi^+\pi^-$ missing mass from a sample of T' hadronic events from CLEO[56] is shown in Fig. 26. Also shown is the missing mass from like-sign $\pi^\pm\pi^\pm$ pairs. The $\pi^+\pi^-$ missing mass distribution shows a clear excess at the mass of the T which is not observed in the like-sign $\pi\pi$ missing mass distribution. (The two distributions are normalized in the mass region outside the T peak.) Also shown in Fig. 26 (dashed curve) is the $\pi^+\pi^-$ missing mass from

$$T' \to \pi^+\pi^- \ell^+\ell^- \quad , \tag{23}$$

where ℓ is either an e or a μ. The T signal is very clean in this topology.

In addition to the CLEO experiment, the $T' \to \pi^+\pi^- T$ transition has also been observed by CUSB[54] and LENA.[67] The results of their measurements are given in Table XIII. In general, except for the CLEO measurement, decays corresponding to process (23) were used for the branching ratio measurements. Note that some measurements may be different than the published values. I have made corrections to the published values based on the measured T leptonic branching ration, $B_{ee}(T) = 3.4 \pm 0.7\%$. Note also that $B_{ee}(T') = 0$ was assumed for all calculations.

Figure 27 shows $\pi^+\pi^-$ invariant mass distributions from CUSB and CLEO based on their sample of events satisfying (23). Both distributions are observed to peak at large values of invariant mass, much like the $\pi\pi$ mass distribution for $\psi' \to \pi\pi J/\psi$ (see Fig. 17). As in the case of the ψ' decays, the distributions are inconsistent with phase space (shown as dashed curves). This has been explained by Brown and Cahn[68] and more

recently by Yan.[69] The solid curve in each case is based on the QCD calculation of Ref. 69 and agrees with the data.

The total widths for the T and T' can be expressed as

$$\begin{aligned} \Gamma_{tot}(T) &= \Gamma_{3g}(T) + \Gamma_{em}(T) \\ \Gamma_{tot}(T') &= \Gamma_{3g}(T') + \Gamma_{2g}(T') + \Gamma_{\gamma P}(T') + \Gamma_{em}(T') \end{aligned} \quad . \tag{24}$$

For simplicity of notation, Γ_{em} now includes both leptonic decays and the second-order electromagnetic decays into hadrons. The 2-gluon transitions at the T' correspond to hadronic transitions from the T' to the T. All contributions from this diagram are expected to be small except for the $\pi\pi$ transition (22). $\Gamma_{\gamma P}(T')$ corresponds to the sum of the radiative transitions to the ^3P states. If it is assumed that α_s is the same at the T and T', then[11,45]

$$\begin{aligned} \Gamma_{3g}(T') + \Gamma_{em}(T') &= \frac{\Gamma_{ee}(T')}{\Gamma_{ee}(T)}\ \Gamma_{tot}(T) \\ &= \frac{\Gamma_{ee}(T')}{B_{ee}(T)} \end{aligned} \quad . \tag{25}$$

From Eqs. (24) and (25)

$$\Gamma_{tot}(T') = \frac{\dfrac{\Gamma_{ee}(T')}{B_{ee}(T)} + \Gamma_{\gamma P}(T')}{1 - \bar{B}(T' \to \pi\pi T)\left(1 - 3B_{ee}(T')\right)} \quad . \tag{26}$$

Remember that the measurements of the branching ratio for (22) were based on $B_{ee}(T') = 0$. This measured branching ratio will be denoted by $\bar{B}(T' \to \pi\pi T)$. The true branching ratio is

$$B(T' \to \pi\pi T) = \bar{B}(T' \to \pi\pi T)\left(1 - 3B_{ee}(T')\right) \quad .$$

This correction is what led to the complicated denominator in Eq. (26). [Note that by isospin $B(T' \to \pi\pi T) = (3/2)B(T' \to \pi^+\pi^- T)$.]

The only unknown in Eq. (26) besides $\Gamma_{tot}(T')$ [remember, $B_{ee}(T') = \Gamma_{ee}(T')/\Gamma_{tot}(T')$] is $\Gamma_{\gamma p}(T')$. The measured value for the ψ' can be scaled[14] to give

$$\Gamma_{\gamma p}(T') \approx \left(\frac{e_b}{e_c}\right)^2 \left(\frac{m_c}{m_b}\right)^2 \Gamma_{\gamma p}(\psi') \approx 4.2 \text{ keV} \quad .$$

To account for the uncertainty in scaling this number, a ±50% error has been included in the calculations. Now Eq. (26) can be solved to give the final widths and branching ratios

$$B_{ee}(T') = 2.0 \pm 0.4 \%$$

$$\Gamma_{ee}(T') = 0.57 \pm 0.04 \text{ keV}$$

$$B(T' \to \pi\pi T) = 27.1 \pm 3.6 \%$$

$$\Gamma_{tot}(T') = 28.8 \pm 6.1 \text{ keV} \quad .$$

Of particular interest is a comparison of the T' total width with the width of the ψ', $\Gamma_{tot}(\psi') = 215 \pm 40$ keV. The reason for this large difference is that most of the large transitions from the ψ' or T' (i.e., the $\pi\pi$ transitions to the J/ψ or T and the E1 radiative transitions) vary as $1/m^2$. Hence, while approximately 90% of ψ' decays go into other charmonium states, it is expected that over half of the T' decays are direct.

A theoretical prediction for the ratio of the partial widths for the decays $T' \to \pi\pi T$ and $\psi' \to \pi\pi$ J/ψ can be made which depends on the spin of the gluon (assuming that 2-gluon exchange is responsible for

the transition). For the case of spin 1 gluons[70]

$$\frac{\Gamma(\Upsilon' \to \pi\pi\Upsilon)}{\Gamma(\psi' \to \pi\pi J/\psi)} \approx \left(\frac{m_c}{m_b}\right)^2 \approx \left(\frac{m_{J/\psi}}{m_\Upsilon}\right)^2 \approx 0.1 \quad .$$

For scalar gluons, the ratio is expected to be near unity.[69] The experimental ratio is 0.072 ± 0.023, consistent with expectations for spin 1 gluons.

Recently, the CLEO collaboration has observed evidence for the transition $\Upsilon'' \to \pi^+\pi^-\Upsilon$, but the results are preliminary.[71] No observations of radiative transitions have yet been reported.

IV. TUPONIUM

In analogy with the three weak isospin lepton doublets (i.e., the e, μ and τ doublets), it is generally expected that a third quark doublet containing the b and a new quark t (for top) exists. There are no firm predictions for the mass of the t quark. However, one can invoke standard numerology based on the ratio of the masses of the $s\bar{s}$, $c\bar{c}$ and $b\bar{b}$ bound states (i.e., $M_{J/\psi}/M_\phi \approx 3$ and $M_\Upsilon/M_{J/\psi} \approx 3$) to predict a mass of 28 GeV for the first $t\bar{t}$ bound state. Other estimates[66] range from 20-150 GeV.

There are a number of methods for establishing the existence of a new quark. First, as discussed in regard to the bottomonium system, an increase in $R = \sigma_{had}/\sigma_{\mu\mu}$ is expected when a new flavor threshold is crossed. From Eq. (21), an increase of 4/3 units of R is expected as t threshold is crossed. Figure 28 shows R as a function of center-of-mass energy up to the highest PETRA energies.[72] (Only statistical errors are shown. Systematic errors are estimated to be approximately ±10%.)

PETRA data from PLUTO, TASSO, Mark J, JADE and CELLO are shown as well as lower energy data from the Mark I,[73] PLUTO[74] and DASP.[75] In order to discriminate hadronic annihilation events from two-photon and beam-gas background, the PETRA experiments require that at least 50% of the total center-of-mass energy is observed in the detector (25% for the case of charged particle detection only). In addition, each event is required to have at least four charged tracks, and $\tau^+\tau^-$ topologies are explicitly removed from the four-track data sample. The quoted cross sections are corrected for acceptance and radiative effects (including hadronic vacuum polarization). The solid curve in Fig. 28 shows the QCD prediction for five quarks (u,d,s,c and b) and the dashed curve shows the six-quark prediction (u,d,s,c,b, and t quarks). These predictions[76] include QCD corrections to second order with

$$R = 3 \sum_{Q=1}^{n_f} e_Q^2 \left[1 + \frac{\alpha_s(s)}{\pi} + \left(1.98 - .115\, n_f\right)\left(\frac{\alpha_s(s)}{\pi}\right)^2 \right]$$

where n_f is the number of quark flavors, $\alpha_s(s) = 12\pi/(33-2n_f)\ \ln(s/\Lambda^2)$, and Λ is the QCD scale parameter. The data is clearly in much better agreement with the five-quark prediction than the six-quark prediction up to the maximum center-of-mass energy of 36.5 GeV.

Table XIV gives the average R values for all data above 20 GeV. The average experimental value agrees quite well with the theoretical expectation. From the variation of the four experimental determinations of R, the error on each measurement can be estimated

$$\sigma = \left[\frac{1}{3}\sum_{i=1}^{4}\left(\bar{R} - R_i\right)^2\right]^{\frac{1}{2}} = 0.16 \quad .$$

This error (approximately 4%) corresponds roughly to the quoted statistical errors. Thus, if ±10% systematic normalization errors are hidden in the data, they have to work at least partly in the same direction in different experiments. Remember, however, that the trigger biases (e.g., the total energy requirement and the charged particle requirement) are similar in all experiments.

It is also expected that the event topology will change significantly when a new flavor threshold is crossed. As the center-of-mass energy increases, events become more and more collimated into jets. Production of a pair of heavy-quark hadrons is expected to lead to an isotropic distribution for a sizable fraction of the events. One measure of the event topology is the sphericity

$$S = \frac{3}{2} \frac{\min \sum_i |p_{\perp i}|^2}{\sum_i |\bar{p}_i|^2} ,$$

where $\bar{p}_i$ are the particle momenta and $p_{\perp i}$ are the transverse momenta relative to the jet axis. Very jet-like events will have sphericities near 0 whereas isotropic events will have sphericities near 1. Thus, the onset of t threshold is expected to result in a significant increase in the average sphericity of events.

Figure 29 shows average sphericity measurements[72] as a function of center-of-mass energy from JADE, PLUTO and TASSO. The distribution is observed to decrease monotonically with energy. The solid curve represents the expected distribution for five quarks and agrees well with

the data. The dashed curve shows the expected increase in sphericity from t decays. There is no evidence for new quark production.

A more sophisticated study incorporates the analysis of the two-dimensional sphericity-aplanarity plot.[77] Aplanarity is defined as

$$A = \frac{3}{2} \frac{\min \sum_i |p_{ni}|^2}{\sum_i |\vec{p}_i|^2} ,$$

where p_{ni} are the particle transverse momenta relative to a plane (rather than relative to an axis as for sphericity). Two-jet and gluon bremsstrahlung events populate the plot in a different manner than $t\bar{t}$ events. An analysis[72] of TASSO, JADE and Mark J events finds that $t\bar{t}$ threshold is excluded by 12 standard deviations at 35.3 GeV and five standard deviations at 36.5 GeV. Note that these limits are based on the assumption that the t quark decays via the sequence $t \to b \to c \to s$ as suggested by the Kobayashi-Maskawa generalized Cabibbo matrix.[78]

Another consequence of this assumed decay scheme is that t decays are a rich source of leptons. An analysis[72] of the yield of muons with momentum greater than 2 GeV by the JADE, Mark J and PLUTO groups shows no evidence of a t quark threshold up to 36.5 GeV.

As in the case of c and b quarks, a series of narrow bound state resonances is expected to precede the t quark threshold. Assuming that the mass of the lowest $t\bar{t}$ bound state is at least 30 GeV, one sees from Fig. 22 that at least six narrow states are expected to be produced. From Fig. 24, assuming the trend of a constant Γ_{ee}/e_Q^2 continues up to the mass of the lowest $t\bar{t}$ bound state, $\Gamma_{ee} \approx 5$ keV for the lowest $t\bar{t}$

bound state. This would lead to a peak with a cross section of approximately seven units of R based on an energy resolution of 20 MeV.

A search for narrow bound states over part of the center-of-mass energy range above 30 GeV has been performed by scanning in 20 MeV steps. A Gaussian curve, corrected for radiative effects,[79] was fitted at each energy point to give an upper limit on $\tilde{\Gamma}_{ee} = \Gamma_{ee}B_{had} = (M^2/6\pi^2)\int\sigma_{had}(M)dM$. Figure 30(a) shows the results of a scan[72] by the JADE, Mark J, PLUTO and TASSO groups from 29.9 to 31.5 GeV. Figure 30(b) shows the results of a similar scan[72] by the JADE, Mark J and TASSO groups from 35.0 to 35.6 GeV. The limits on $\tilde{\Gamma}_{ee}$ are given in Table XV. JADE has also presented results[80] on a scan over the entire center-of-mass region from 33.0 to 36.72 GeV. They set an upper limit of $\tilde{\Gamma}_{ee} < 1.3$ keV (90% confidence level) over this entire range.

These experimental limits are all considerably lower than the naive theoretical prediction. [Note that the theoretical prediction is for Γ_{ee} whereas the experimental limits are for $\tilde{\Gamma}_{ee}$. However, it is expected that B_{had} is at least 90% and hence $\Gamma_{ee} \approx \tilde{\Gamma}_{ee}$.] Thus, experimental results seem to rule out the existence of a narrow bound state with charge 2/3 in the energy range which has been scanned.

The possibility exists that there are narrow bound states in the center-of-mass energy regions which have not yet been scanned. However, from Fig. 22, it is expected that the threshold for t production is approximately 2 GeV above the mass of the lowest $t\bar{t}$ bound state (assuming a bound state in the neighborhood of 30-40 GeV). There is no evidence for a threshold below 36.5 GeV, and no evidence for a bound state between 33.0 and 36.5 GeV (a range of 3.5 GeV). Thus, it is

likely that there is no bound state for a charge 2/3 quark below 36.5 GeV. Limits for an additional charge -1/3 quark are not convincing.

REFERENCES

1. J. J. Aubert et al., Phys. Rev. Lett. 33, 1404 (1974).
2. J.-E. Augustin et al., Phys. Rev. Lett. 33, 1406 (1974).
3. G. S. Abrams et al., Phys. Rev. Lett. 33, 1453 (1974).
4. S. W. Herb et al., Phys. Rev. Lett. 39, 252 (1977).
5. W. R. Innes et al., Phys. Rev. Lett. 39, 1240 (1977).
6. Ch. Berger et al., Phys. Lett. 76B, 243 (1978).
7. C. W. Darden et al., Phys. Lett. 76B, 246 (1978).
8. R. Partridge et al., Phys. Rev. Lett. 45, 1150 (1980).
9. K. Königsmann, in High Energy Physics - 1980, eds. L. Durand and L. G. Pondrom (AIP, New York, 1981), p. 675.
10. T. M. Himel et al., Phys. Rev. Lett. 45, 1146 (1980).
11. T. Appelquist and H. D. Politzer, Phys. Rev. Lett. 34, 43 (1975).
12. A. DeRújula and S. L. Glashow, Phys. Rev. Lett. 34, 46 (1975).
13. T. Appelquist, R. M. Barnett and K. Lane, Ann. Rev. Nucl. Part. Sci. 28, 387 (1978).
14. E. Eichten, K. Gottfried, T. Kinoshita, K. D. Lane and T. M. Yan, Phys. Rev. D21, 203 (1980).
15. T. M. Himel et al., Phys. Rev. Lett. 44, 920 (1980).
16. M. J. Oreglia, Stanford Linear Accelerator Center Report No. SLAC-236, Ph.D. Thesis, Stanford University, 1980 (unpublished).
17. T. M. Himel, Stanford Linear Accelerator Center Report No. SLAC-223, Ph.D Thesis, Stanford University, 1979 (unpublished).
18. J. S. Whitaker et al., Phys. Rev. Lett. 37, 1596 (1976).

19. B. H. Wiik and G. Wolf, Electron-Positron Interactions (Springer-Verlag, New York, 1979).

20. W. Bartel et al., Phys. Lett. 79B, 492 (1978).

21. Particle Data Group, Rev. Mod. Phys. 52, S1 (1980).

22. T. Burnett, presented at the Irvine Conference on Color, Flavor and Unification, Irvine, California, 1979 (unpublished).

23. J. Gaiser, private communication.

24. A. B. Henriques, B. H. Kellett and R. G. Moorhouse, Phys. Lett. 64B, 85 (1976)

25. J. D. Jackson, in Weak Interactions at High Energies and the Production of New Particles, ed. M. C. Zipf (Stanford, California, 1976), p. 147.

26. W. Tanenbaum et al., Phys. Rev. D17, 1731 (1978).

27. M. Oreglia et al., Phys. Rev. Lett. 45, 959 (1980).

28. W. Tanenbaum et al., Phys. Rev. Lett. 36, 402 (1976).

29. R. Brandelik et al., Nucl. Phys. B160, 426 (1979).

30. H. Harari, Phys. Lett. 60B, 172 (1975).

31. H. Fritzsch and J. D. Jackson, Phys. Lett. 66B, 365 (1977).

32. H. Goldberg, Phys. Rev. Lett. 44, 363 (1980).

33. G. Segre and J. Weyers, Phys. Lett. 62B, 91 (1976).

34. N. Deshpande and E. Ma, Phys. Lett. 69B, 341 (1977).

35. H. Ganz, Nuovo Cim. Lett. 21, 270 (1978).

36. R. Bhandari and L. Wolfenstein, Phys. Rev. D17, 1857 (1978).

37. P. Langacker, Phys. Lett. 90B, 447 (1980).

38. N. Isgur, H. R. Rubinstein, A. Schwimmer and H. J. Lipkin, Phys. Lett. 89B, 79 (1979).

39. B. L. Ioffe and M. A. Shifman, Phys. Lett. 95B, 99 (1980).

40. D. Andrews et al., Phys. Rev. Lett. 44, 1108 (1980).

41. D. Andrews et al., Phys. Rev. Lett. 45, 219 (1980).

42. T. Böhringer et al., Phys. Rev. Lett. 44, 1111 (1980).

43. G. Finocchiaro et al., Phys. Rev. Lett. 45, 222 (1980).

44. R. Van Royen and V. F. Weisskopf, Nuovo Cimento 50A, 617 (1967).

45. T. Appelquist and H. D. Politzer, Phys. Rev. D12, 1404 (1975).

46. J. K. Bienlein et al., Phys. Lett. 78B, 360 (1978).

47. H. Schröder, in Experimental Meson Spectroscopy - 1980, eds. S. U. Chung and S. J. Lindenbaum (AIP, New York, 1981), p. 356.

48. B. Niczyporuk et al., Phys. Rev. Lett. 46, 92 (1981).

49. B. Niczyporuk et al., Phys. Lett. 99B, 169 (1981).

50. E. H. Thorndike, in High Energy Physics - 1980, eds. L. Durand and L. G. Pondrom (AIP, New York, 1981), p. 705.

51. Ch. Berger et al., Z. Phys. C1, 343 (1979).

52. P. Bock et al., Z. Phys. C6, 125 (1980).

53. H. Albrecht et al., Phys. Lett. 93B, 500 (1980).

54. G. Mageras et al., Phys. Rev. Lett. 46, 1115 (1981).

55. Ch. Berger et al., Phys. Lett. 93B, 497 (1980).

56. J. J. Mueller et al., Phys. Rev. Lett. 46, 1181 (1981).

57. C. Quigg and J. L. Rosner, Phys. Lett. 71B, 153 (1977).

58. A. Martin, in High Energy Physics - 1980, eds. L. Durand and L. G. Pondrom (AIP, New York, 1981), p. 715.

59. G. Ehanot and S. Rudaz, Phys. Lett. 78B, 119 (1978).

60. J. L. Richardson, Phys. Lett. 82B, 272 (1979).

61. W. Buchmüller, G. Grunberg and S.-H. H. Tye, Phys. Rev. Lett. 45, 103 (1980).

62. C. Quigg and J. L. Rosner, Phys. Lett. 72B, 462 (1978).

63. E. Eichten and K. Gottfried, Phys. Lett. 66B, 286 (1977).

64. J. L. Rosner, C. Quigg and H. B. Thacker, Phys. Lett. 74B, 350 (1978).

65. J. Lee-Franzini, Cornell Report No. CLNS 81/488, 1981 (submitted for publication to Surveys High Energy Phys.).

66. M. Krammer, H. Krasemann and S. Ono, DESY Report No. DESY 80/25, 1980 (submitted for publication to Z. Phys. C).

67. B. Niczyporuk et al., Phys. Lett. 100B, 95 (1981).

68. L. Brown and R. Cahn, Phys. Rev. Lett. 35, 1 (1975).

69. T. M. Yan, Phys. Rev. D 22, 1652 (1980).

70. K. Gottfried, Phys. Rev. Lett. 40, 598 (1978).

71. K. Berkelman, public communication.

72. D. Cords, in High Energy Physics - 1980, eds. L. Durand and L. G. Pondrom (AIP, New York, 1981), p. 590.

73. J. L. Siegrist, Stanford Linear Accelerator Center Report No. SLAC-225, Ph.D. Thesis, Stanford University, 1979 (unpublished).

74. Ch. Berger et al., Phys. Lett. 81B, 410 (1979).

75. R. Brandelik et al., Phys. Lett. 76B, 361 (1978).

76. M. Dine and J. Sapirstein, Phys. Rev. Lett. 43, 668 (1979).

77 R. Brandelik et al., Z. Phys. C4, 87 (1980).

78. N. Kobayashi and T. Maskawa, Prog. Theor. Phys. 49, 652 (1973).

79. J. D. Jackson and D. L. Scharre, Nucl. Instr. Meth. 128, 13 (1975).

80. W. Bartel et al., Phys. Lett. 100B, 364 (1981).

TABLE I. η_c branching ratio measurements (Mark I).

Decay Mode	$B(\psi' \to \gamma\eta_c) \times B(\eta_c \to X)$	$B(\eta_c \to X)^a$
$p\bar{p}$	$\left(8\ ^{+8}_{-4}\right)\times 10^{-6}$	$.2\ ^{+\ .2}_{-\ .1}$ %
$\pi^+\pi^-\pi^+\pi^-$	$\left(5.7\ ^{+3.9}_{-2.4}\right)\times 10^{-5}$	$1.3\ ^{+1.1}_{-1.8}$ %
$\pi^+\pi^-K^+K^-$	$\left(4.0\ ^{+6.0}_{-2.5}\right)\times 10^{-5}$	$.9\ ^{+1.4}_{-\ .7}$ %
$\pi^+\pi^-p\bar{p}$	$< 5\times 10^{-5}$ [b]	< 1 % [b]
$K^\pm\pi^\mp K^0_S$	$\left(1.5\ ^{+\ .8}_{-\ .6}\right)\times 10^{-4}$	$3.5\ ^{+2.5}_{-2.1}$ %

[a] Based on $B(\psi' \to \gamma\eta_c)$ from Crystal Ball.
[b] 90% confidence level.

TABLE II. χ mass measurements.

State	Mass (MeV) [a]		
	Mark II [b]	Crystal Ball [c]	Average
χ(3415)	3412.9 ± 0.6		3412.9 ± 0.6
χ(3510)	3508.1 ± 0.6	3508.4 ± 0.4	3508.3 ± 0.3
χ(3550)	3555.3 ± 1.1	3553.9 ± 0.5	3554.1 ± 0.5

[a] There is an overall ±4 MeV uncertainty on all measurements due to the uncertainty in the absolute energy normalization. All masses are based on 3095.0 for the mass of the J/ψ.

[b] Reference 17.

[c] Reference 16.

TABLE III. $\psi' \to \gamma\chi$, $\chi \to \gamma J/\psi$ branching ratio measurements.

Experiment	$B(\psi' \to \gamma\chi) \times B(\chi \to \gamma J/\psi)$ (%)		
	$\chi(3550)$	$\chi(3510)$	$\chi(3415)$
Mark I [a]	1.0 ± 0.6	2.4 ± 0.8	0.2 ± 0.2
DASP [b]	1.6 ± 0.4	2.1 ± 0.4	0.3 ± 0.2
DESY-Heidelberg [c]	1.0 ± 0.2	2.5 ± 0.4	0.14 ± 0.09
Mark II [d]	1.1 ± 0.3	2.4 ± 0.6	< 0.56 [e]
Crystal Ball [f]	1.26 ± 0.22	2.38 ± 0.40	0.06 ± 0.02
Average	1.16 ± 0.12	2.34 ± 0.21	0.07 ± 0.02

[a] Reference 18.
[b] Reference 19.
[c] Reference 20.
[d] Reference 17.
[e] 90% confidence level.
[f] Reference 16.

TABLE IV. $\chi \rightarrow \gamma J/\psi$ branching ratio measurements.

State	$B(\chi \rightarrow \gamma J/\psi)$ (%)
$\chi(3415)$	1.0 ± 0.4
$\chi(3510)$	33 ± 10
$\chi(3550)$	17 ± 5

TABLE V. χ total and radiative widths.

State	Γ_{tot} (MeV)	$\Gamma(\chi \to \gamma J/\psi)$ (keV)	
		Experiment	Theory [a]
χ(3415)	10 ± 3	100 ± 50	~ 100
χ(3510)	< 2 [b]	< 700 [b]	200–300
χ(3550)	≤ 4 ± 1	≤ 680 ± 260	300–400

[a] References 14, 24 and 25.
[b] 1-σ upper limit.

TABLE VI. χ spin determinations.

State	Spin Hypothesis	Confidence Level
$\chi(3550)$	0	5×10^{-4}
	1	0.01
	2	0.11
$\chi(3510)$	0	$< 10^{-6}$
	1	0.13
	2	0.02

TABLE VII. $\psi' \to \eta J/\psi$ branching ratio measurements.

Experiment	Branching Ratio (%)
Mark I [a]	4.3 ± 0.8
DASP [b]	3.5 ± 0.9
DESY-Heidelberg [c]	3.6 ± 0.5
Mark II [d]	2.5 ± 0.6
Crystal Ball [e]	2.18 ± 0.38
Average	2.9 ± 0.3

[a] Reference 28.
[b] Reference 29.
[c] Reference 20.
[d] Reference 15
[e] Reference 27.

TABLE VIII. Υ resonance masses (experimental).

Experiment	M_Υ(MeV)	$M_{\Upsilon'} - M_\Upsilon$(MeV)	$M_{\Upsilon''} - M_\Upsilon$(MeV)	$M_{\Upsilon'''} - M_\Upsilon$(MeV)
PLUTO	9460±10[a]			
DESY[b]	9460±10[c]	560±10[c]		
DASP II	9463.1±0.7±10[d]	553.7±1.7±10[d]		
LENA	9461.6±0.6±10[e]	552.0±1.3±10[f]		
CLEO	9433.6±0.2±28[g]	560.8±0.4±3[g]	889.5±0.5±4[g]	1114.0±1.1±5[g]
CUSB	9434.5±0.4±28[h]	559±1±3[h]	889±1±5[h]	1114±2±5[i]
Average	9462.2±10[j,k] 9433.8±28[m]	559.9±2.9[l]	889.4±4.0	1114.0±5.1

[a] Reference 6.
[b] DESY-Hamburg-Heidelberg-MPI München.
[c] Reference 46.
[d] Reference 47.
[e] Reference 48.
[f] Reference 49.
[g] Reference 50.
[h] Reference 42.
[i] Reference 43.
[j] DORIS only.
[k] PLUTO and DESY results are not used in this average.
[l] DESY results are not used in this average.
[m] CESR only.

TABLE IX. Υ resonance reduced leptonic widths (experimental).

Experiment	$\tilde{\Gamma}_{ee}(\Upsilon)$ (keV)	$\tilde{\Gamma}_{ee}(\Upsilon')/\Gamma_{ee}(\Upsilon)$	$\tilde{\Gamma}_{ee}(\Upsilon'')/\Gamma_{ee}(\Upsilon)$	$\tilde{\Gamma}_{ee}(\Upsilon''')/\Gamma_{ee}(\Upsilon)$
PLUTO	1.24±0.13[a,b]			
DESY[c]	1.00±0.23[d]	0.33±0.16[d,e]		
DASP II	1.23±0.22[f]	0.45±0.10[g]		
LENA	1.10±0.13[h]	0.43±0.07[i]		
CLEO	0.925±0.15[j]	0.46±0.07[j]	0.28±0.05[j]	0.22±0.04[j]
CUSB	0.97±0.16[a,k]	0.46±0.05[k]	0.29±0.04[l]	0.23±0.06[m]
Average	1.08±0.06	0.45±0.03	0.29±0.03	0.22±0.03

[a] Calculated by me based on quoted values of Γ_{ee} and B_{ee} from experiment.
[b] Reference 51.
[c] DESY-Hamburg-Heidelberg-MPI München
[d] Reference 52.
[e] Calculated by me; no relative systematic errors dropped in the ratio.
[f] Reference 53.
[g] Reference 47.
[h] Reference 48.
[i] Reference 49.
[j] Reference 50.
[k] Reference 54.
[l] Reference 42.
[m] Reference 43.

TABLE X. Υ leptonic branching ratio.

Experiment	$B_{\mu\mu}$ (%)	B_{ee} (%)
PLUTO	2.2±2.0[a]	5.1±3.0[b]
DASP II	2.9±1.4[c]	
LENA	3.5±1.5[d]	
CLEO		3.9±1.1[e]
Average	3.4±0.7[f]	

[a] Reference 51.
[b] Reference 55.
[c] Reference 53.
[d] Reference 48.
[e] Reference 56.
[f] $B_{\mu\mu}$ and B_{ee} are combined.

TABLE XI. Resonance masses and leptonic widths (comparison of experiment with theory).

Parameter	Experiment	Potential Model				
		logarithmic[a]	power law[b]	Coulomb + linear[c]	Coulomb + logarithmic + linear[d]	QCD[e]
$M_{\psi'} - M_{\psi}$ (MeV)	588±1	(589)	(589)	(589)	(586)	595
$M_{\Upsilon'} - M_{\Upsilon}$ (MeV)	560±3	590	(560)	(560)	561–566[f]	(560)
$M_{\Upsilon''} - M_{\Upsilon}$ (MeV)	889±4	910	890	898	881–879[f]	890
$M_{\Upsilon'''} - M_{\Upsilon}$ (MeV)	1114±5	1140	1130	1170	1141–1123[f]	1130
$\Gamma_{ee}(\psi')/\Gamma_{ee}(\psi)$	0.45±0.06	0.36	0.35	0.44	(.44)	0.45
$\Gamma_{ee}(\Upsilon')/\Gamma_{ee}(\Upsilon)$	0.48±0.03	0.45	0.43	0.39	0.44–0.43[f]	0.45
$\Gamma_{ee}(\Upsilon'')/\Gamma_{ee}(\Upsilon)$[g]	0.29±0.03	0.29	0.2[illegible]	0.27	0.32–0.29[f]	0.32
$\Gamma_{ee}(\Upsilon''')/\Gamma_{ee}(\Upsilon)$[g]	0.22±0.03	0.22	0.20	0.23	0.27–0.24[f]	0.26

[a] Reference 57.
[b] Reference 58.
[c] Reference 14.
[d] Reference 59.
[e] Reference 61.
[f] Range of values depends on quark mass assumed.
[g] Experimental numbers are based on the assumption $B_{ee} = 0$.

TABLE [illegible]I. Gaussian widths of T resonances (CLEO).

Resonance	σ (MeV)
T	3.14 ± 0.20
T'	3.53 ± 0.22
T''	3.76 ± 0.24
T'''	9.00 ± 0.82

TABLE XIII. $\Upsilon' \to \pi^+\pi^-\Upsilon$ branching ratio measurements.

Experiment	$B(\Upsilon' \to \pi^+\pi^-\Upsilon)$ (%)
CLEO[a]	19.1 ± 3.1
CUSB[b]	19 ± 6
LENA[c]	20 ± 7
Average	19.2 ± 2.6

[a] Reference 56.
[b] Reference 54.
[c] Reference 67.

TABLE XIV. Hadronic cross section measurements for W ≥ 20 GeV (PETRA).

Experiment	$R = \sigma_{had}/\sigma_{\mu\mu}$
JADE	3.84 ± 0.10
Mark J	4.17 ± 0.10
PLUTO	3.82 ± 0.14
TASSO	4.00 ± 0.13
Average	3.97 ± 0.06
Theory[a]	3.92 ± 0.06

[a] Calculation is based on W = 30 GeV and $\alpha_s = 0.20 \pm 0.04$ with five quarks.

TABLE XV. Limits on $\tilde{\Gamma}_{ee}$ for narrow resonance production at high energy (PETRA).

W (GeV)	$\tilde{\Gamma}_{ee}$ (keV)
29.9 - 31.5	$< 0.7^{a,b}$
35.0 - 35.6	$< 0.4^{a,b}$
33.0 - 36.72	$< 1.3^{b,c}$
Theory	$\sim 5^{d}$

[a] Reference 72.
[b] 90% confidence level.
[c] Reference 80.
[d] B_{had} is assumed to be approximately 1.

FIGURE CAPTIONS

Fig. 1. Charmonium level diagram showing states as a function of J^{PC}. Solid lines indicate established states or transitions. Dashed lines indicate unobserved states or transitions.

Fig. 2. Inclusive photon spectrum from ψ' hadronic decays (Crystal Ball).

Fig. 3. Inclusive photon spectrum from J/ψ hadronic decays (Crystal Ball).

Fig. 4. Inclusive photon spectrum from the ψ' in the region of the η_c transition (Crystal Ball): a) unsubtracted and b) background subtracted spectra are shown. Curves show result of best fit to combined ψ' and J/ψ spectra.

Fig. 5. Inclusive photon spectrum from the J/ψ in the region of the η_c transition (Crystal Ball): a) unsubtracted and b) background subtracted spectra are shown. Curves show result of best fit to combined ψ' and J/ψ spectra.

Fig. 6. Fitted photon energy for events which satisfy the hypothesis $J/\psi \to \gamma\pi^+\pi^-$ (Crystal Ball).

Fig. 7. Fitted hadronic mass distribution for direct-photon transitions from the ψ' (Mark II).

Fig. 8. Low $\gamma J/\psi$ mass vs. high $\gamma J/\psi$ mass for events which satisfy the hypothesis $\psi' \to \gamma\gamma J/\psi$ (Mark II). Also shown are the $\gamma J/\psi$ mass projections. Curve represents fit to data.

Fig. 9. Low $\gamma J/\psi$ mass vs. high $\gamma J/\psi$ mass for events which satisfy the hypothesis $\psi' \to \gamma\gamma J/\psi$ (Crystal Ball).

Fig. 10. $\psi' \to \gamma\gamma J/\psi$ Dalitz plot (Crystal Ball).

Fig. 11. $\gamma J/\psi$ invariant mass projection (Crystal Ball). Solid curve is fit to the data. Dashed curve is one hundred times the expected background from $\psi' \to \pi^0\pi^0 J/\psi$.

Fig. 12. Hadronic invariant mass distributions for the processes a) $\psi' \to \gamma 2\pi^+ 2\pi^-$ and b) $\psi' \to \gamma 3\pi^+ 3\pi^-$ (Mark II). Curves represent fits to the data.

Fig. 13. Photon energy spectrum for $\psi' \to \gamma\gamma J/\psi$ (Crystal Ball). Curves represent fits to spectrum and are described in text.

Fig. 14. $\cos\theta_\gamma$ angular distributions for a) $\chi(3550)$, b) $\chi(3510)$ and c) $\chi(3415)$ (Crystal Ball). Curves show results of best fits for specified spin hypotheses.

Fig. 15. $\gamma\gamma$ invariant mass distribution for $\psi' \to \gamma\gamma J/\psi$ (Mark II). Curve is the expected background from $\psi' \to \pi^0\pi^0 J/\psi$.

Fig. 16. $\gamma\gamma$ invariant mass distributions for $\psi' \to \gamma\gamma J/\psi$ (Crystal Ball). a) Curve is ten times the expected background from $\psi' \to \pi^0\pi^0 J/\psi$. b) Distribution after elimination of $\psi' \to \gamma\chi$, $\chi \to \gamma J/\psi$ and $\psi' \to \eta J/\psi$ events.

Fig. 17. $\pi\pi$ invariant mass squared distribution for $\psi' \to \pi^+\pi^- J/\psi$ (solid points—Mark II) and $\psi' \to \pi^0\pi^0 J/\psi$ (open points—Crystal Ball). Dashed curve shows expected phase space distribution.

Fig. 18. Bottomonium level diagram showing states as a function of J^{PC}. Solid lines indicate established states or transitions. Dashed lines indicate unobserved states or transitions.

Fig. 19. Hadronic cross section as a function of center-of-mass energy showing the Υ, Υ' and Υ'' resonances observed by a) CLEO and b) CUSB.

Fig. 20. Hadronic cross section as a function of center-of-mass energy showing the Υ'' and Υ''' resonances observed by a) CLEO and b) CUSB. A thrust cut ($T > 0.8$) has been applied to CUSB data.

Fig. 21. Potentials of References 57 (logarithmic), 58 (power law), 14 (Coulomb + linear), 59 (Coulomb + log + linear), and 61 (QCD-modified Richardson). Mean radii for ^3S states in the ψ and Υ systems are also shown.

Fig. 22. Heavy quark continuum threshold as a function of m_Q/m_c relative to the ^3S levels.

Fig. 23. $\Gamma_{ee}(\Upsilon)$ vs. $\Gamma_{ee}(\Upsilon')$ as measured experimentally. Also shown are allowed regions for charge 2/3 and charge -1/3 quarks.

Fig. 24. Γ_{ee}/e_Q^2 vs. mass for known vector meson resonances.

Fig. 25. R as a function of mass in the region of the Υ''' (CUSB). Solid curve shows fit to distribution below and on the resonance. Dashed curve shows fit above the resonance.

Fig. 26. Missing mass from $\Upsilon' \to \pi\pi\nu\bar{\nu}$ recoiling against opposite-sign pions (data points) and like-sign pions (solid histogram) from CLEO (left ordinate). Curve is a fit to the data. Dashed histogram represents $\pi^+\pi^-$ missing mass from $\Upsilon' \to \pi^+\pi^-\ell^+\ell^-$ (right ordinate).

Fig. 27. $\pi^+\pi^-$ invariant mass distributions for $\Upsilon' \to \pi^+\pi^-\ell^+\ell^-$ from a) CUSB and b) CLEO ($x = M_{\pi\pi}/2m_\pi$).

Fig. 28. R as a function of center-of-mass energy W. Curves are described in text.

Fig. 29. Average sphericity as a function of center-of-mass energy W. Curves are described in text.

Fig. 30. Energy scan showing combined R data for a) JADE, Mark J, PLUTO and TASSO for $29.9 \leq W \leq 31.5$ GeV and b) JADE, Mark J and TASSO for $35.0 \leq W \leq 35.6$ GeV.

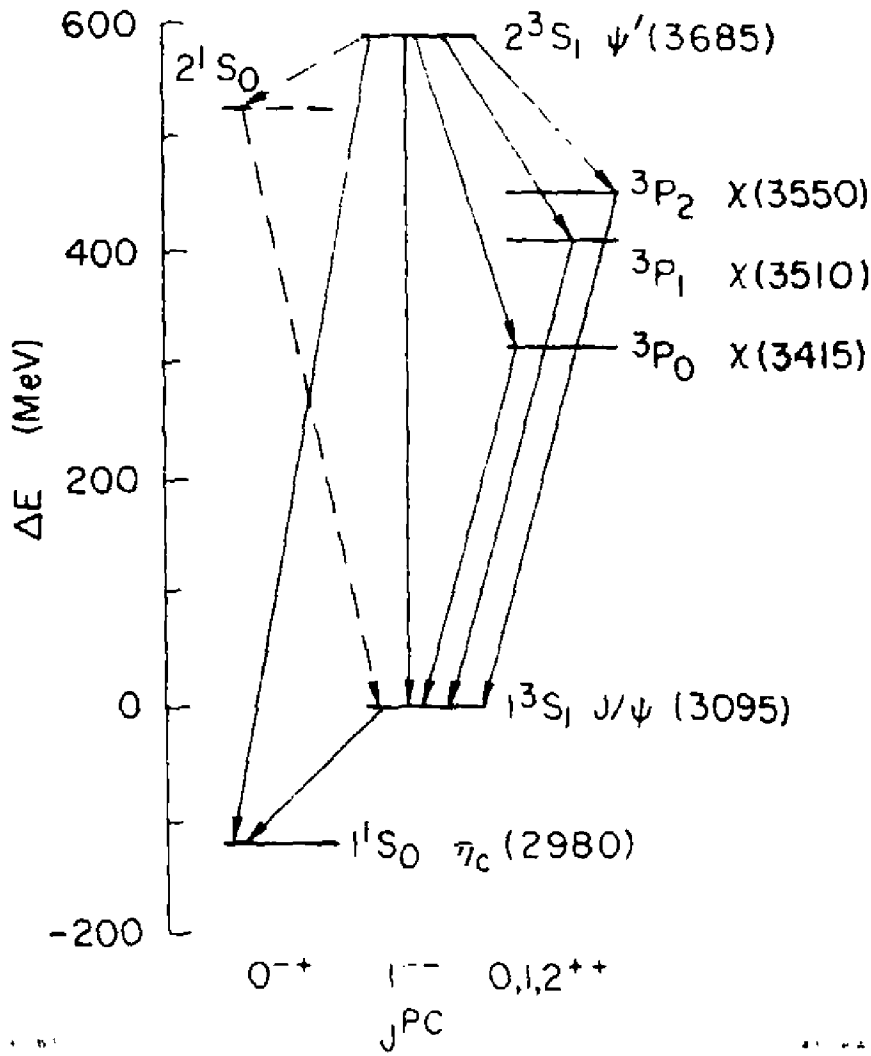
600
400
200
0
-200
ΔE (MeV)
2^1S_0
2^3S_1 ψ'(3685)
$^3P_2$ χ(3550)
$^3P_1$ χ(3510)
$^3P_0$ χ(3415)
1^3S_1 J/ψ (3095)
1^1S_0 η_c (2980)
0^{-+} 1^{--} $0,1,2^{++}$
J^{PC}

Fig 1

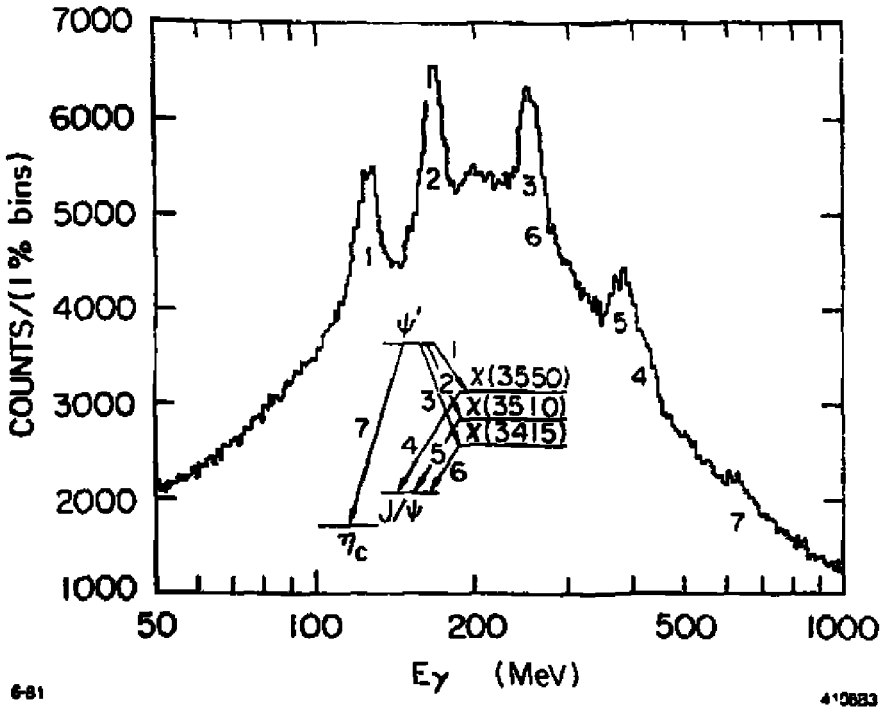
7000
6000
5000
4000
3000
2000
1000
COUNTS/(1% bins)
50
100
200
500
1000
Eγ (MeV)
ψ'
J/ψ
ηc
X(3550)
X(3510)
X(3415)
1
2
3
4
5
6
7
6-81
410883

Fig. 2

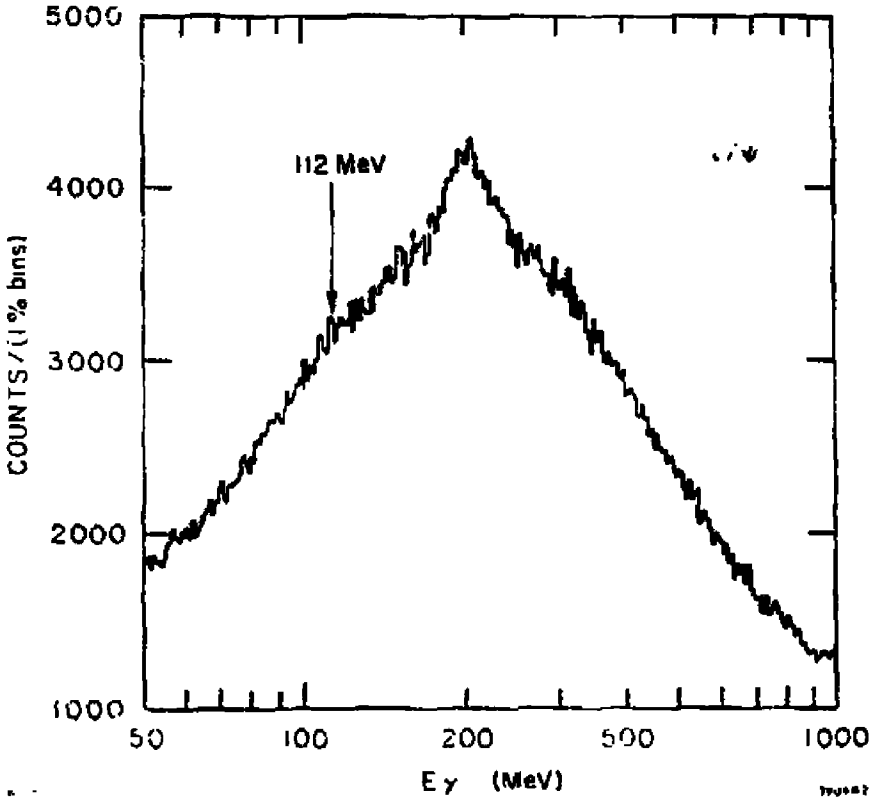
5000
4000
3000
2000
1000
112 MeV
COUNTS/(1% bins)
50
100
200
500
1000
Eγ (MeV)

Fig 3

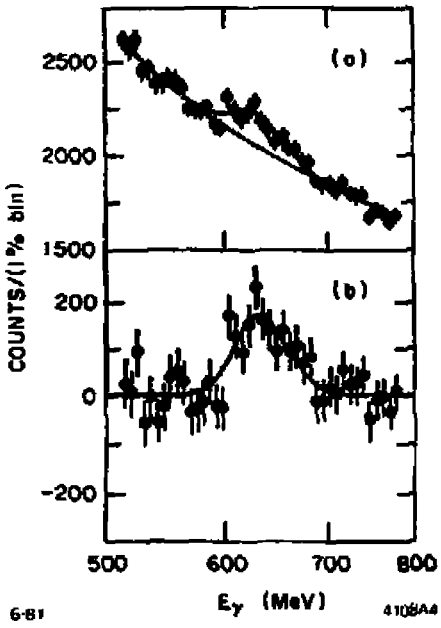
(a)
(b)
2500
2000
1500
200
0
-200
COUNTS/(1% bin)
500
600
700
800
Eγ (MeV)
6-81
4108A4

Fig. 4

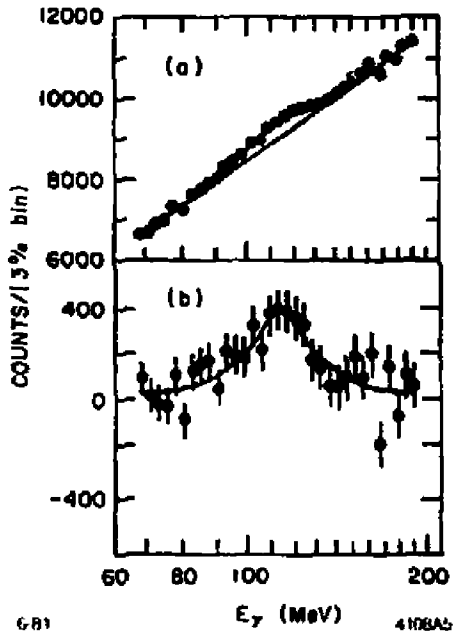
12000
10000
8000
6000
(a)
400
0
-400
(b)
COUNTS/(3% bin)
60
80
100
200
E_γ (MeV)

Fig. 5

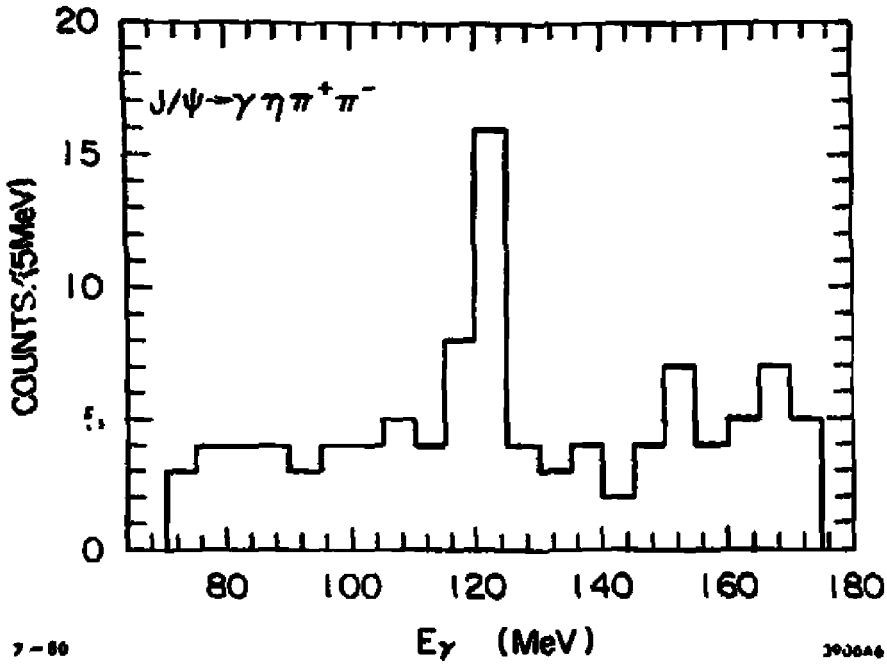
20
15
10
5
0
COUNTS/(5MeV)
$J/\psi \to \gamma\eta\pi^+\pi^-$
80
100
120
140
160
180
E_γ (MeV)

Fig. 6

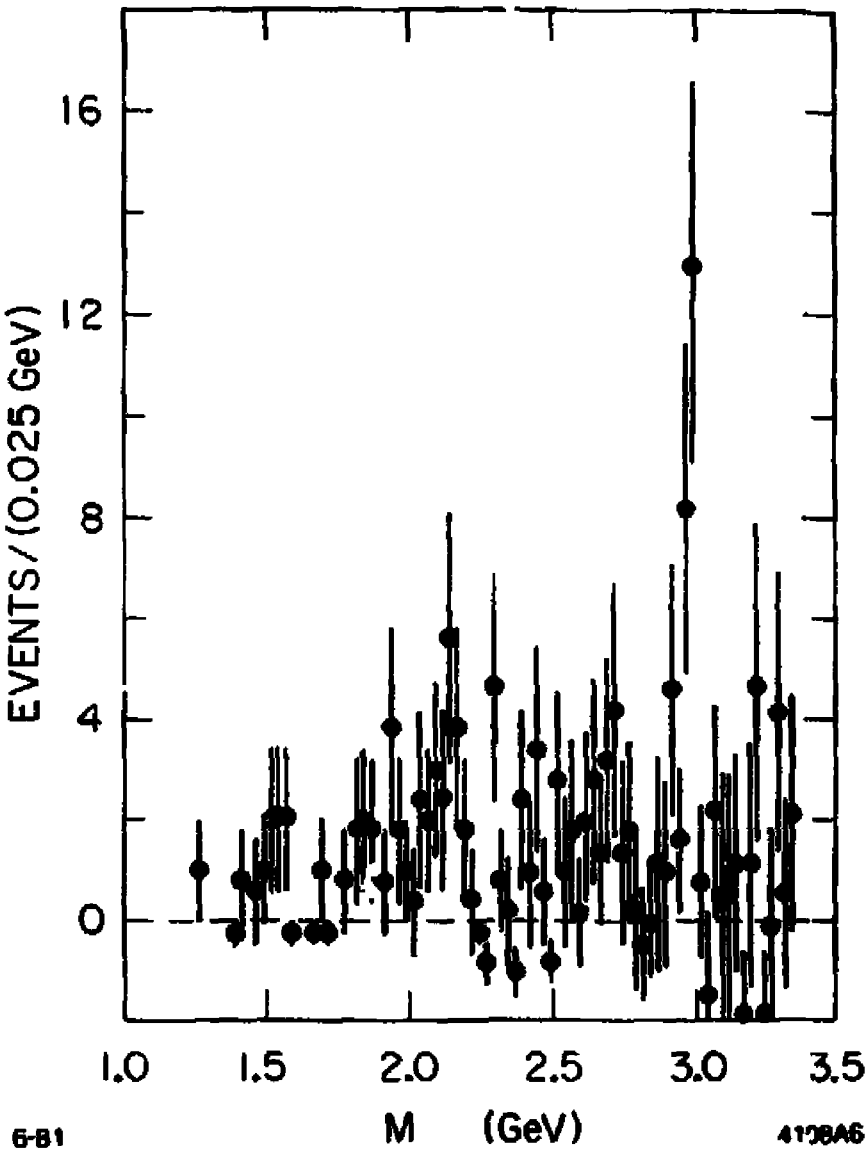

Fig. 7

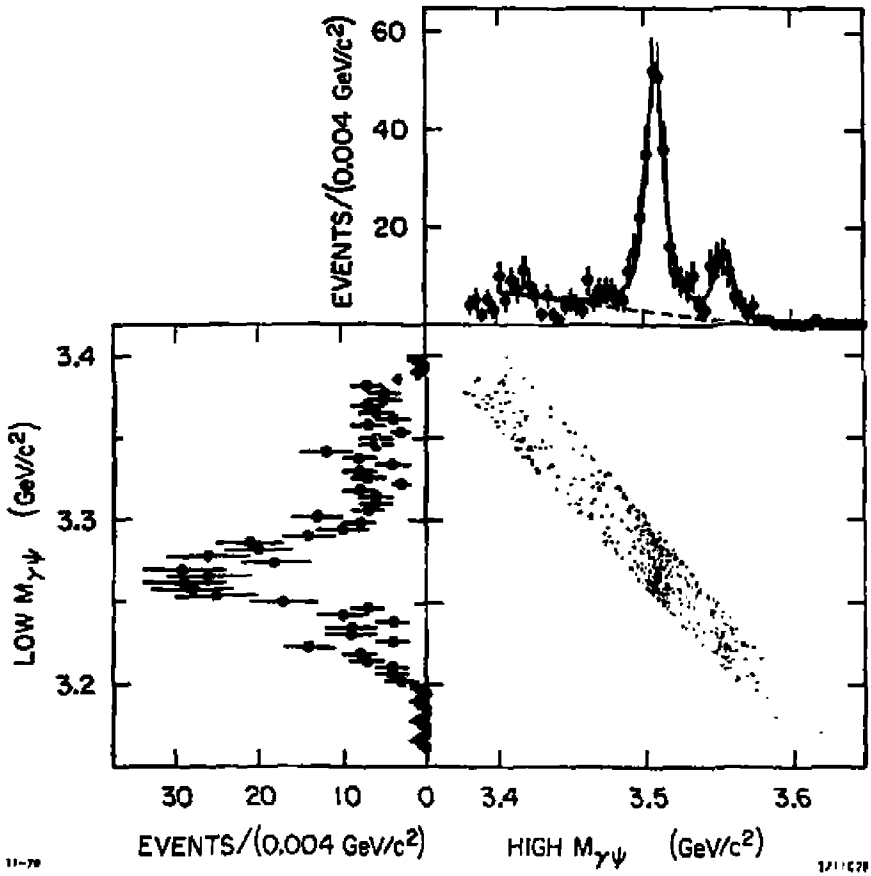
EVENTS/(0.004 GeV/c²)
60
40
20
LOW M$_{\gamma\psi}$ (GeV/c²)
3.4
3.3
3.2
30
20
10
0
EVENTS/(0.004 GeV/c²)
3.4
3.5
3.6
HIGH M$_{\gamma\psi}$ (GeV/c²)

Fig. 8

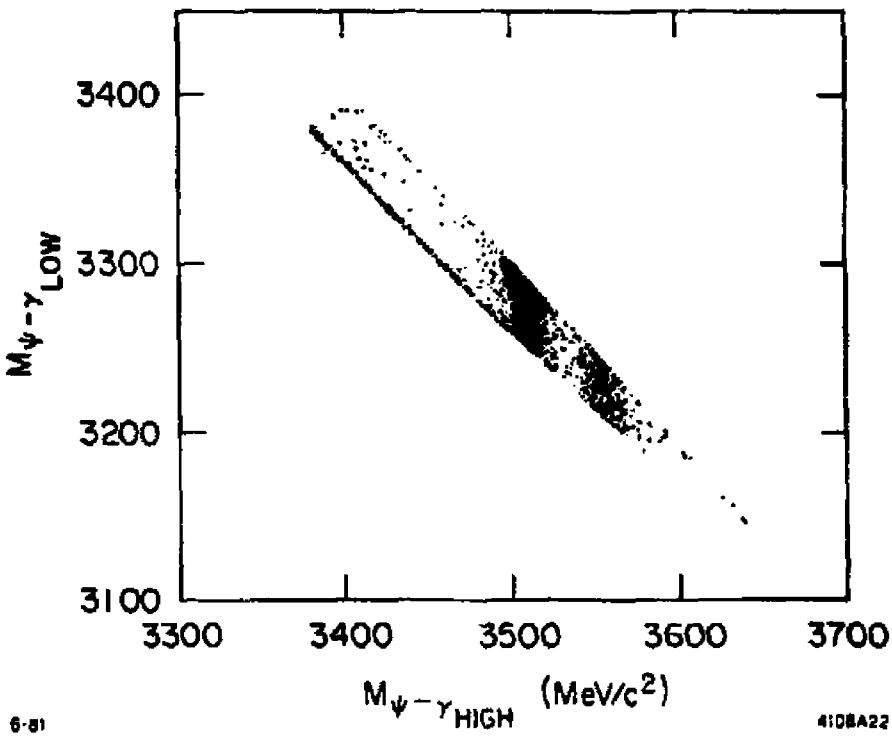
3400
3300
3200
3100
$M_{\psi-\gamma_{LOW}}$
3300
3400
3500
3600
3700
$M_{\psi-\gamma_{HIGH}}$ (MeV/c^2)
6-81
4108A22

Fig. 9

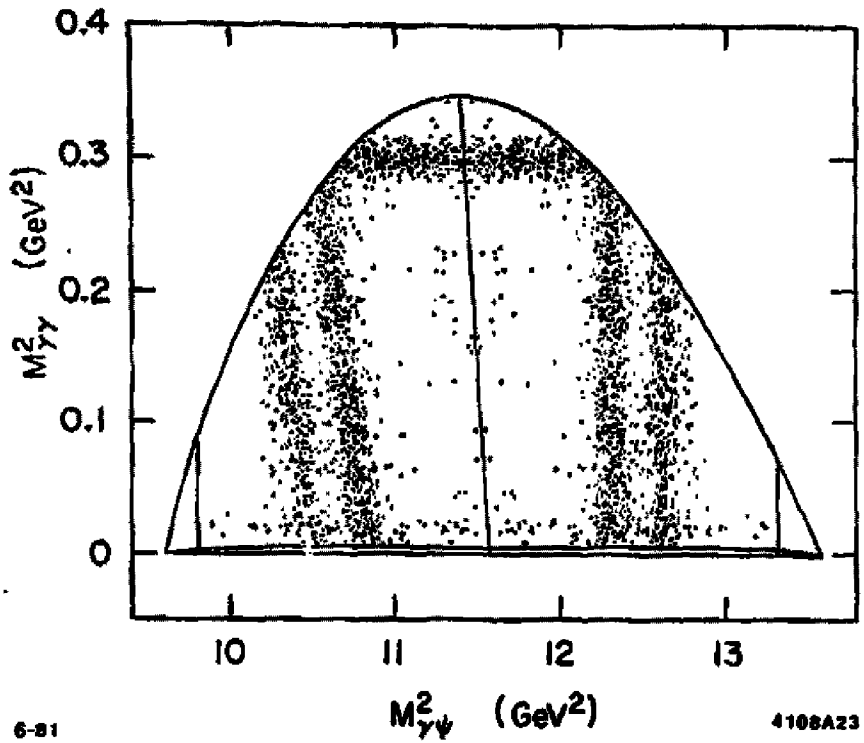
0.4
0.3
0.2
0.1
0
$M^2_{\gamma\gamma}$ (GeV^2)
10
11
12
13
$M^2_{\gamma\psi}$ (GeV^2)
6-81
4108A23

Fig. 10

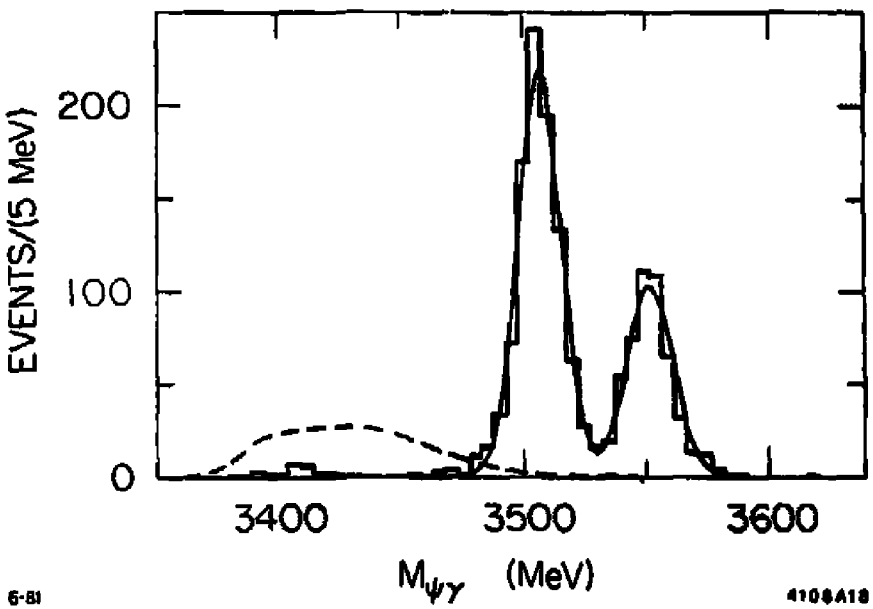
EVENTS/(5 MeV)
200
100
0
3400
3500
3600
$M_{\psi\gamma}$ (MeV)
6-81
4108A18

Fig. 11

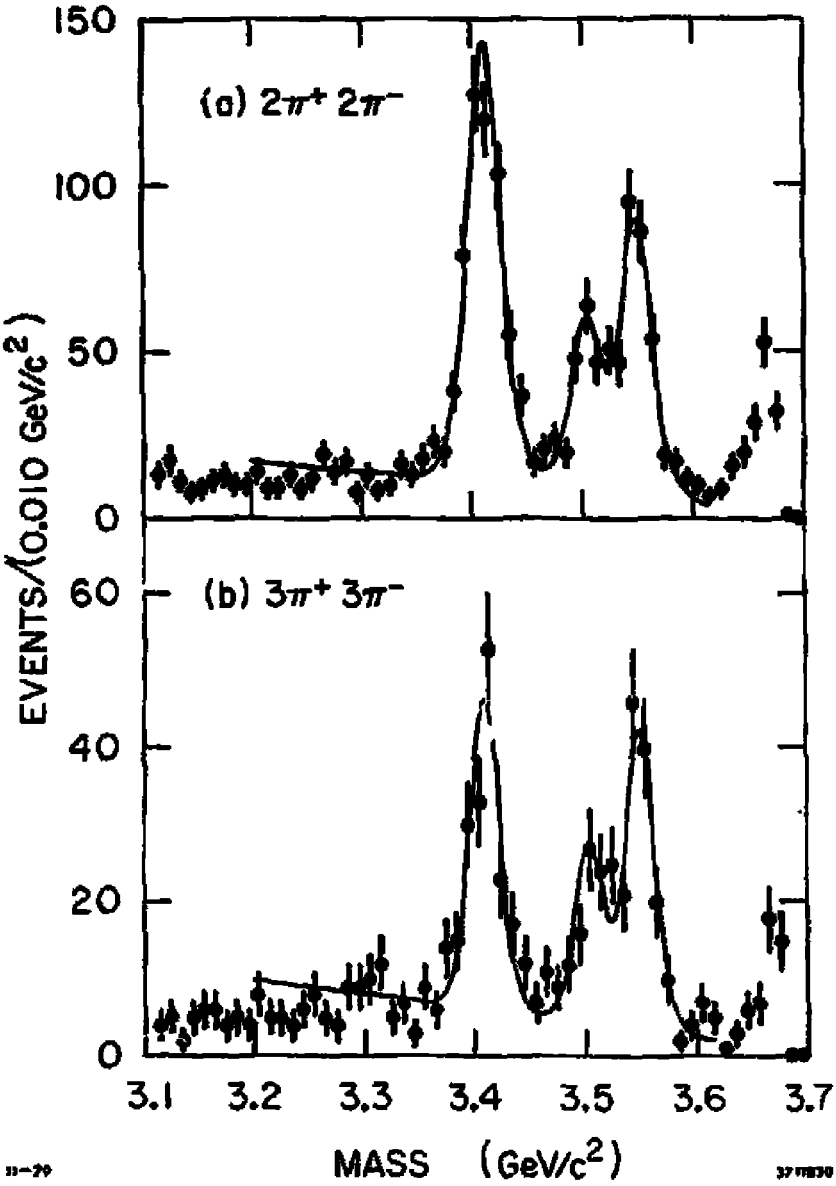
150
100
50
0
(a) 2π+ 2π−
60
40
20
0
(b) 3π+ 3π−
EVENTS/(0.010 GeV/c²)
3.1
3.2
3.3
3.4
3.5
3.6
3.7
MASS (GeV/c²)

Fig. 12

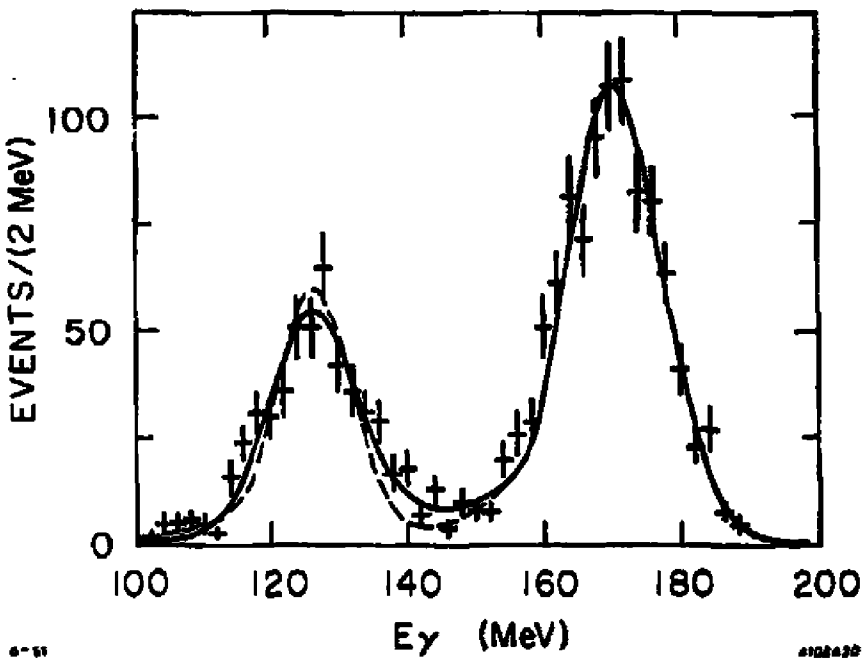

Fig. 13

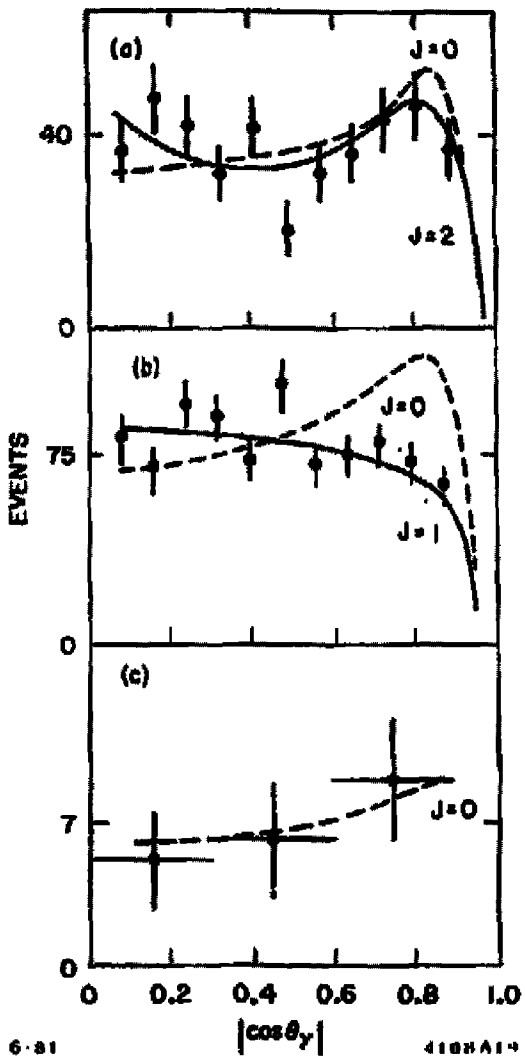
(a)
J=0
J=2
40
0
(b)
J=0
J=1
75
0
EVENTS
(c)
J=0
7
0
0
0.2
0.4
0.6
0.8
1.0
$|\cos\theta_y|$
6-81

Fig. 14

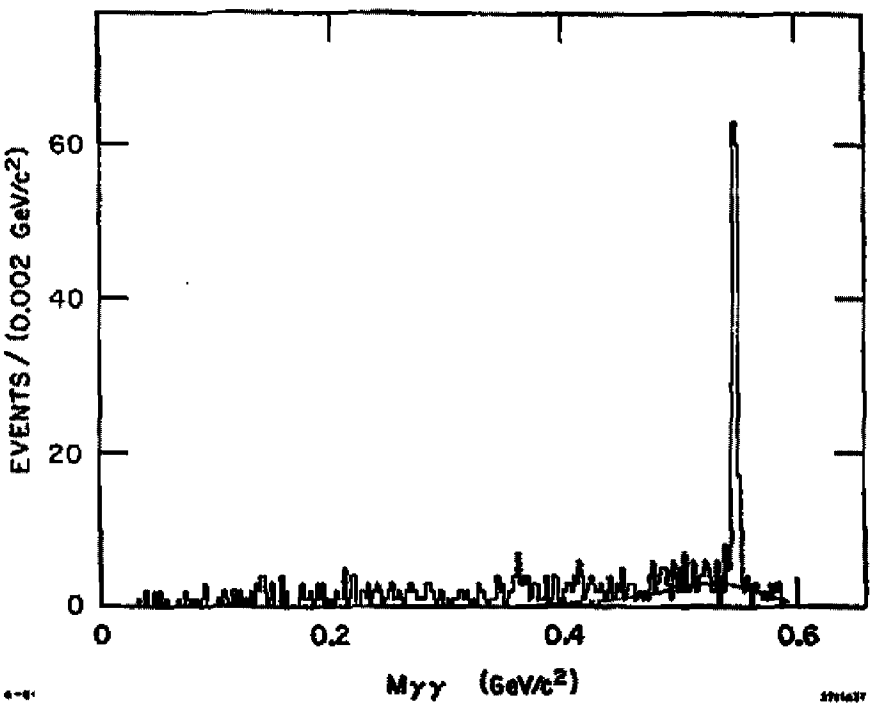

Fig. 15

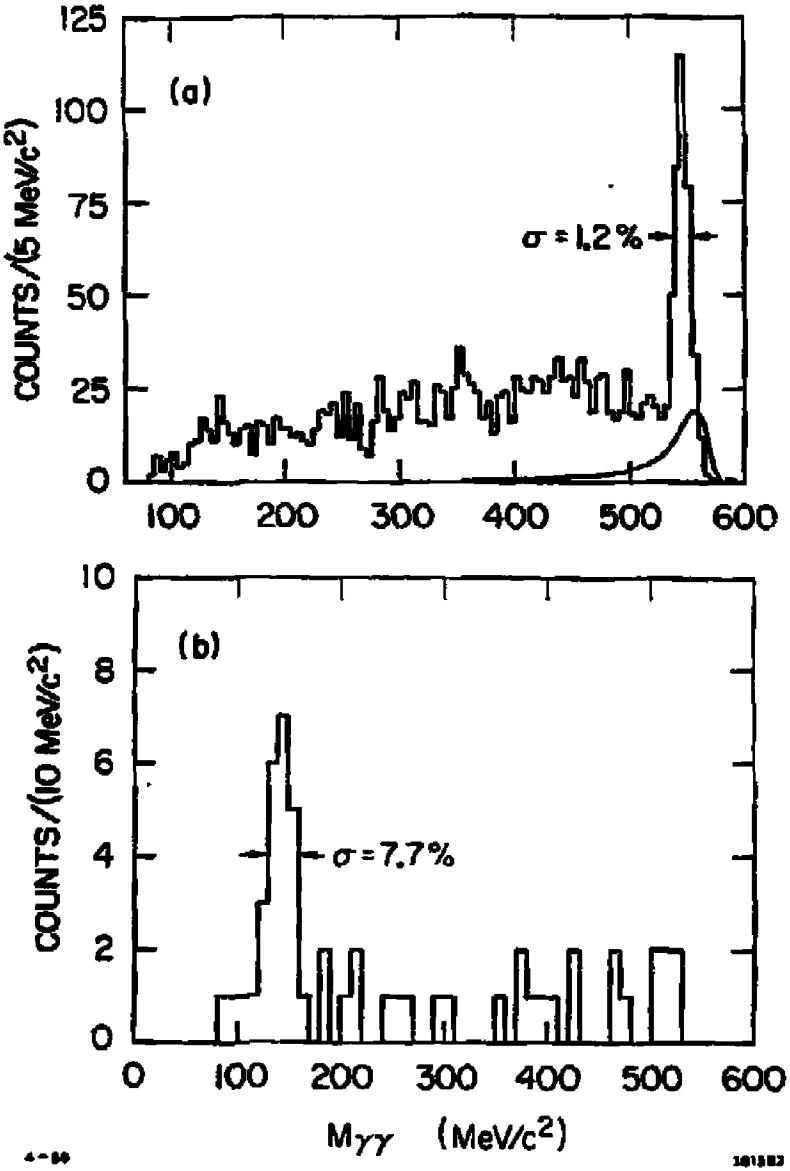
(a)
σ = 1.2%
COUNTS/(5 MeV/c²)
125
100
75
50
25
0
100
200
300
400
500
600
(b)
σ = 7.7%
COUNTS/(10 MeV/c²)
10
8
6
4
2
0
0
100
200
300
400
500
600
Mγγ (MeV/c²)

Fig. 16

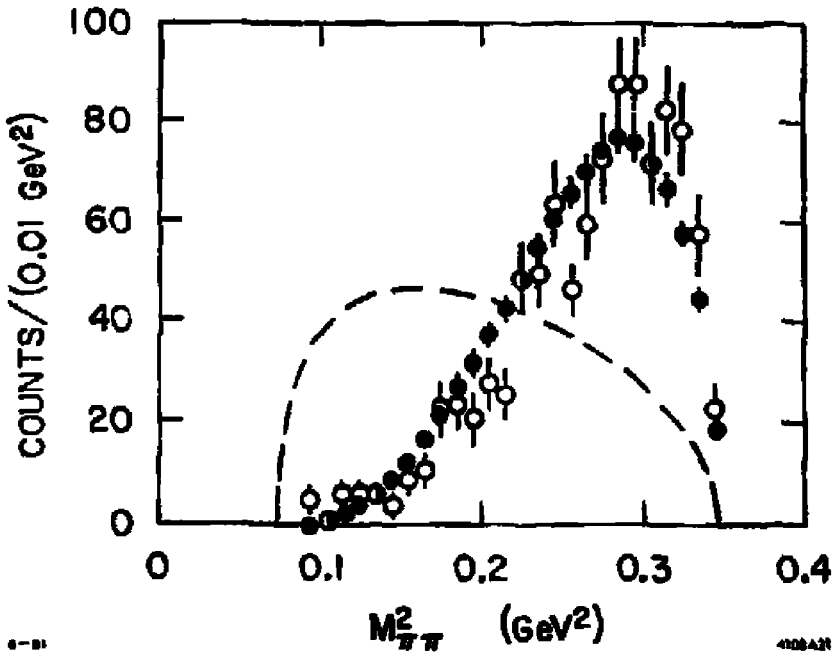

Fig. 17

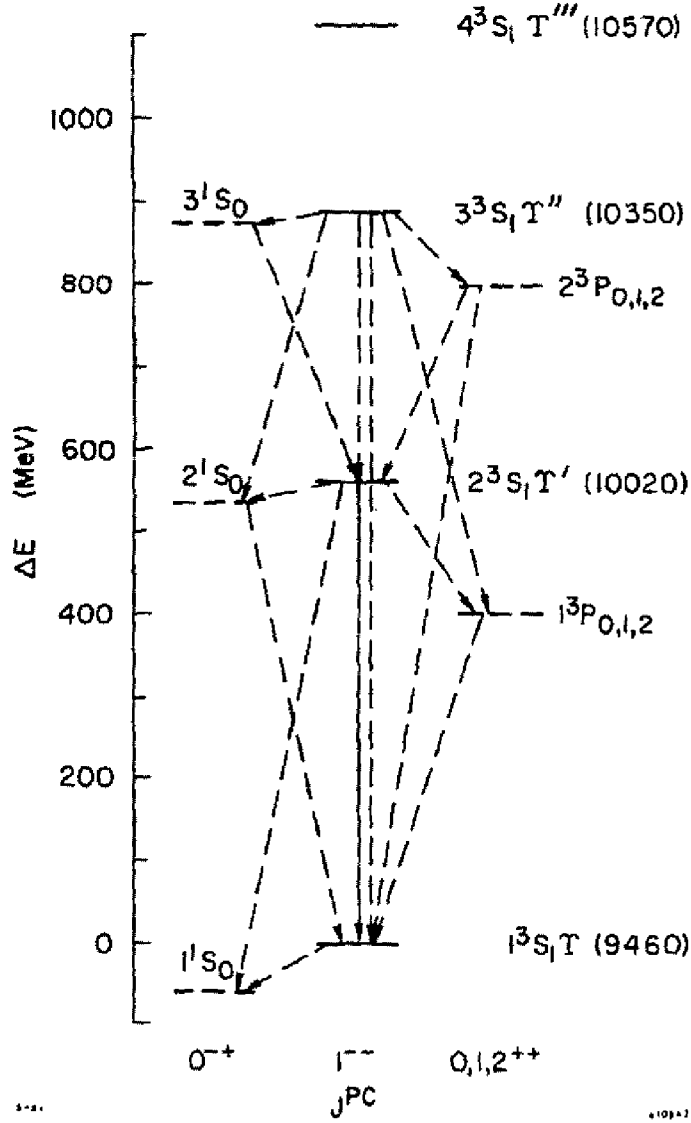
$4^3S_1\ T'''(10570)$
1000
3^1S_0
$3^3S_1\ T''$ (10350)
800
$2^3P_{0,1,2}$
600
2^1S_0
$2^3S_1\ T'$ (10020)
ΔE (MeV)
400
$1^3P_{0,1,2}$
200
0
1^1S_0
$1^3S_1\ T$ (9460)
0^{-+}
1^{--}
$0,1,2^{++}$
J^{PC}

Fig. 18

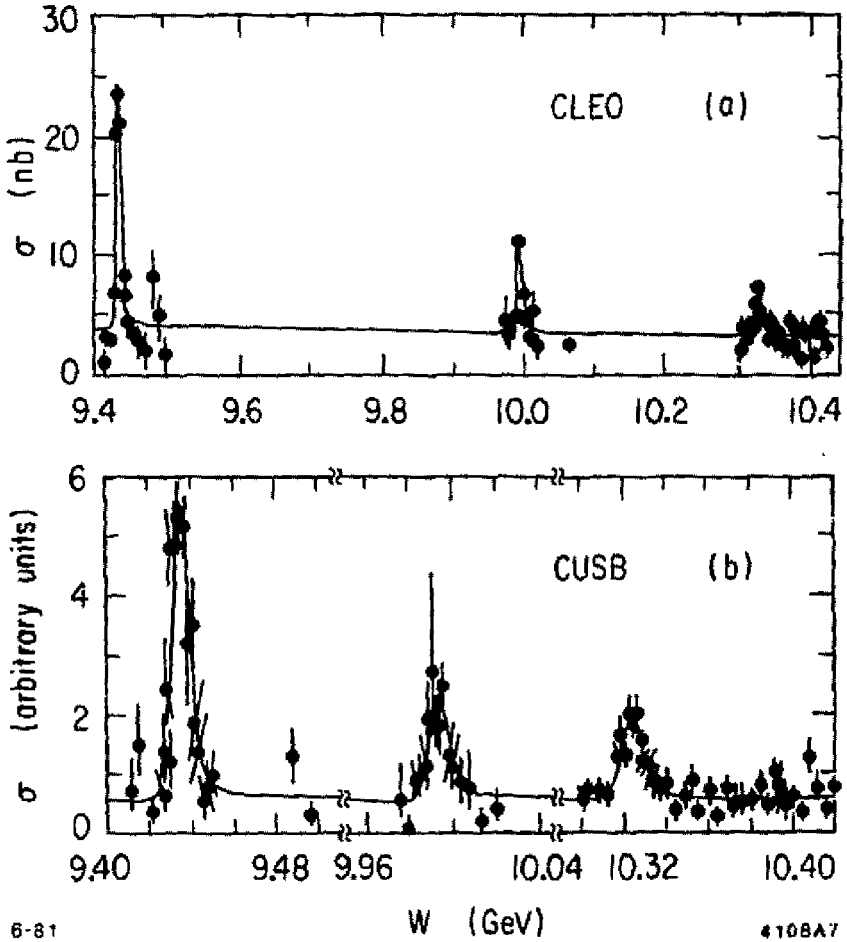
30
20
10
0
σ (nb)
CLEO (a)
9.4
9.6
9.8
10.0
10.2
10.4
6
4
2
0
σ (arbitrary units)
CUSB (b)
9.40
9.48
9.96
10.04
10.32
10.40
W (GeV)
6-81
4108A7

Fig. 19

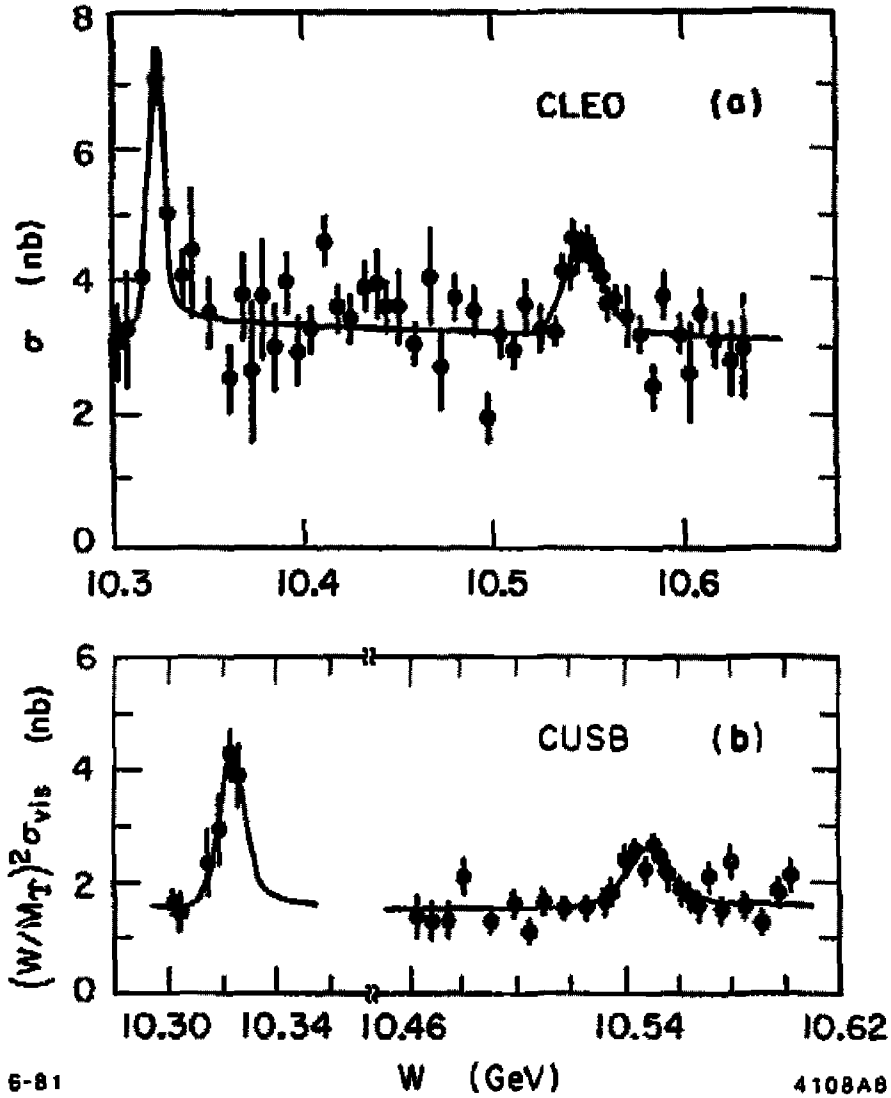
CLEO (a)
σ (nb)
8
6
4
2
0
10.3
10.4
10.5
10.6
CUSB (b)
$(W/M_\Upsilon)^2\sigma_{vis}$ (nb)
6
4
2
0
10.30
10.34
10.46
10.54
10.62
W (GeV)
6-81
4108A8

Fig. 20

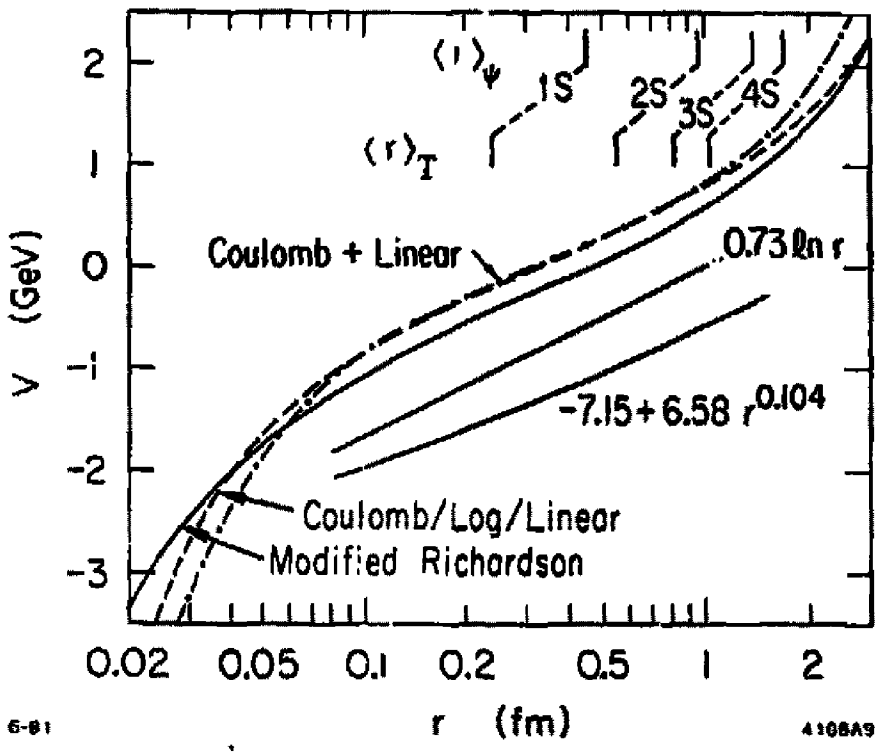
2
1
0
-1
-2
-3
V (GeV)
⟨r⟩ψ
1S
2S
3S
4S
⟨r⟩T
Coulomb + Linear
0.73 ln r
-7.15+6.58 r^0.104
Coulomb/Log/Linear
Modified Richardson
0.02
0.05
0.1
0.2
0.5
1
2
r (fm)
6-81
4108A9

Fig. 21

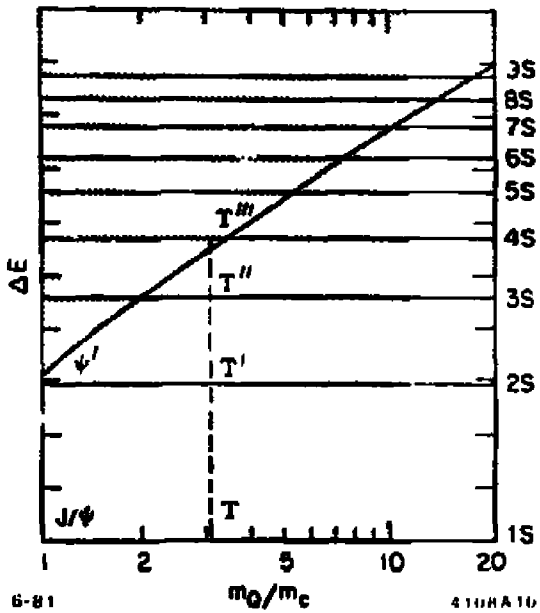

Fig. 22

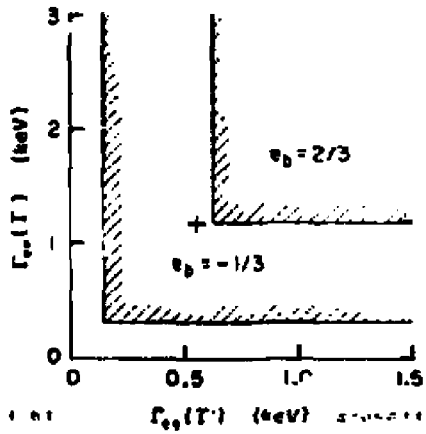

Fig. 23

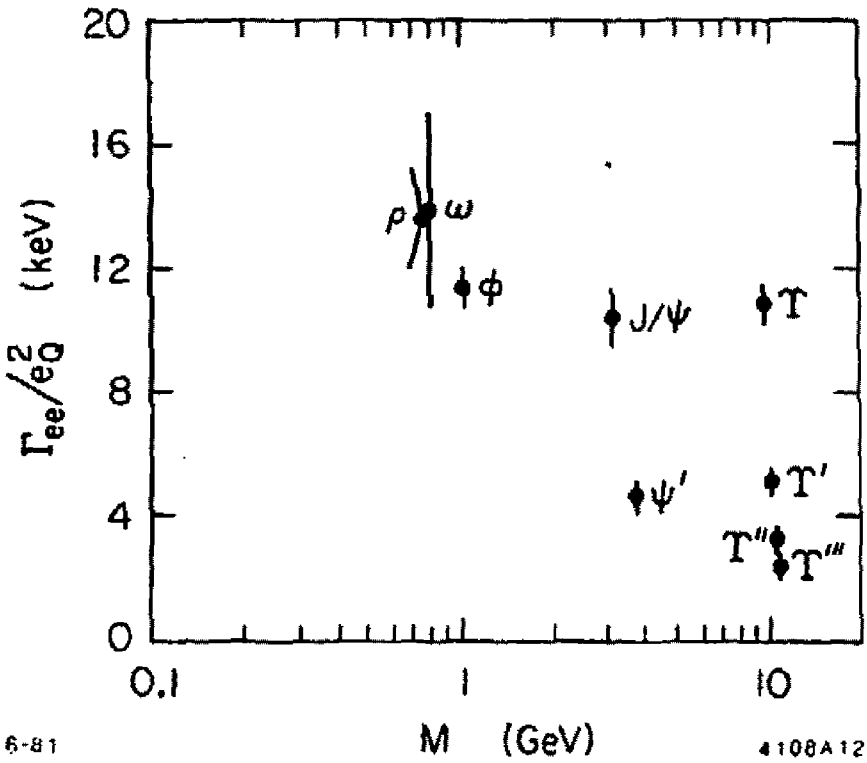
20
16
12
8
4
0
Γ_{ee}/e_Q^2 (keV)
0.1
1
10
M (GeV)
ρ
ω
φ
J/ψ
ψ′
Υ
Υ′
Υ″
Υ‴
6-81
4108A12

Fig. 24

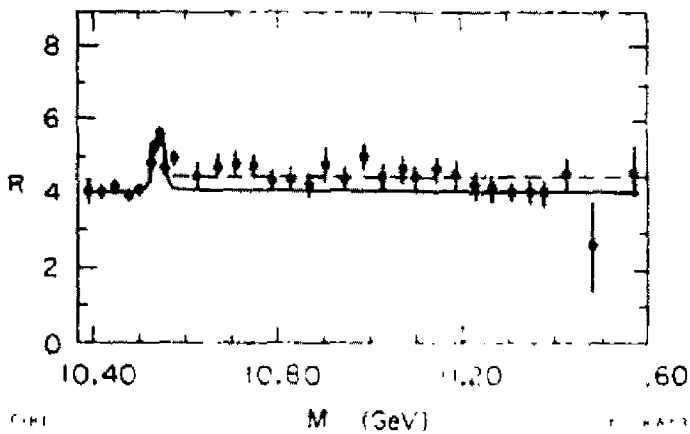

Fig 25

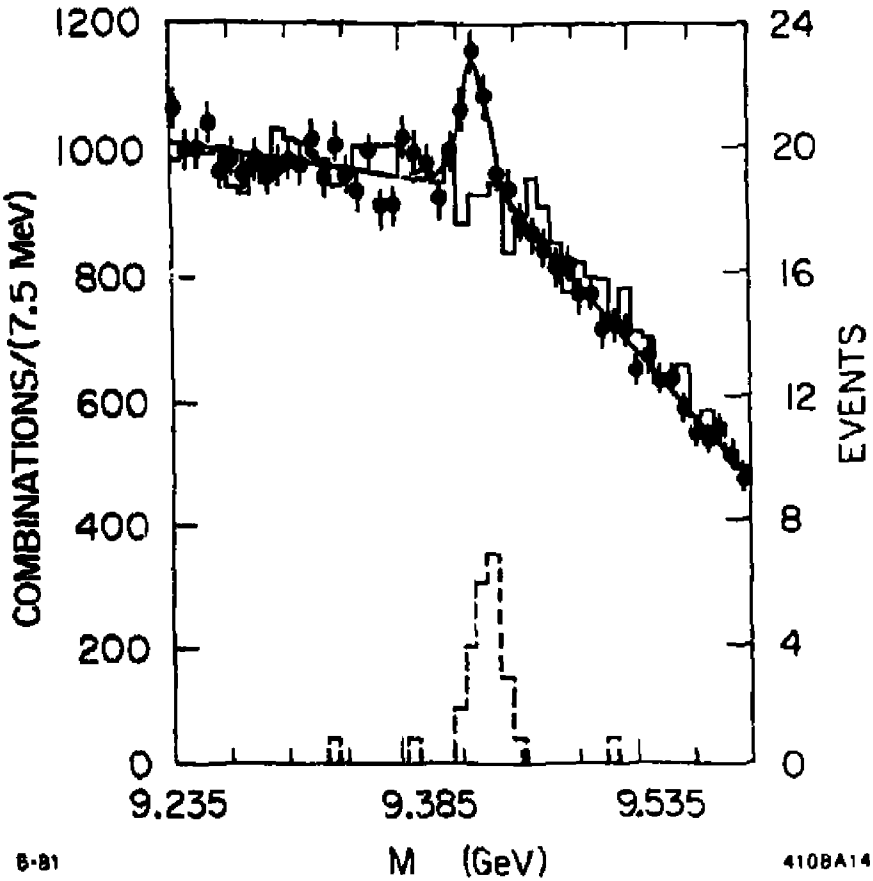
1200
1000
800
600
400
200
0
COMBINATIONS/(7.5 MeV)
24
20
16
12
8
4
0
EVENTS
9.235
9.385
9.535
M (GeV)
6-81
410BA14

Fig. 26

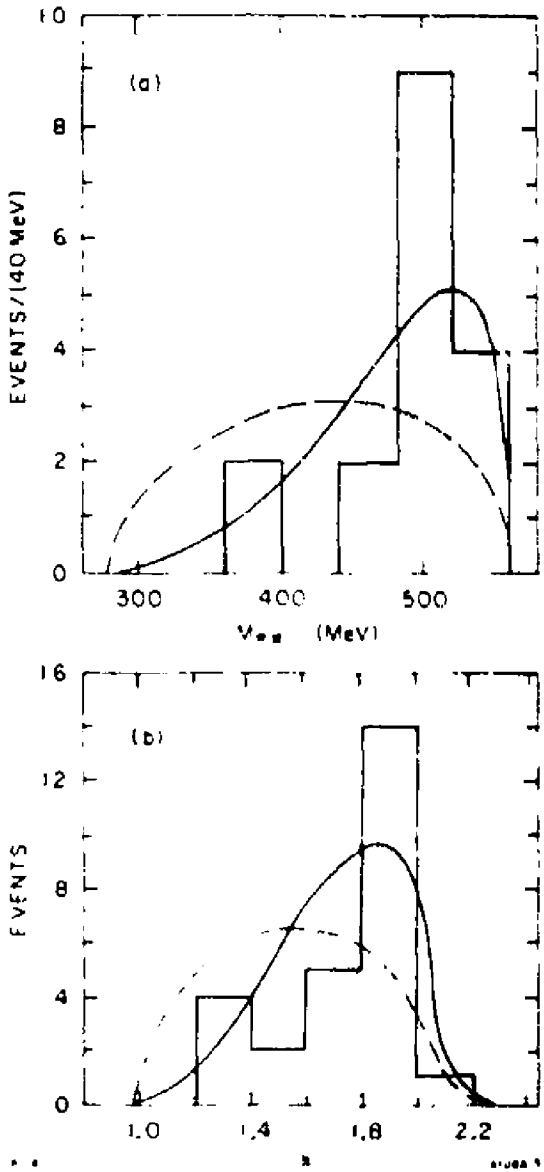
(a)
EVENTS/(40 MeV)
10
8
6
4
2
0
300
400
500
(MeV)
(b)
EVENTS
16
12
8
4
0
1.0
1.4
1.8
2.2

Fig. 27

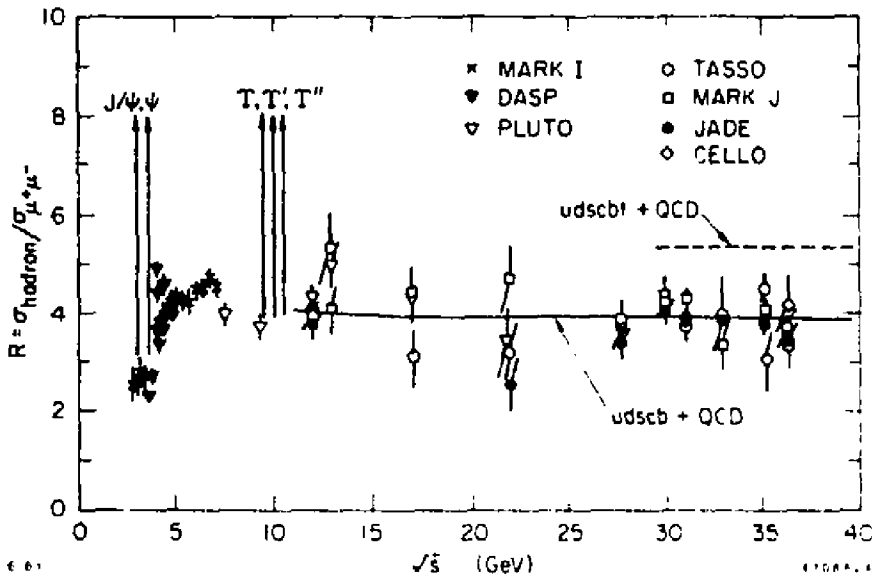
MARK I
DASP
PLUTO
TASSO
MARK J
JADE
CELLO
J/ψ,ψ
T,T',T''
udscbt + QCD
udscb + QCD
R = σhadron/σμ+μ-
√s (GeV)
0
2
4
6
8
10
0
5
10
15
20
25
30
35
40

Fig. 28

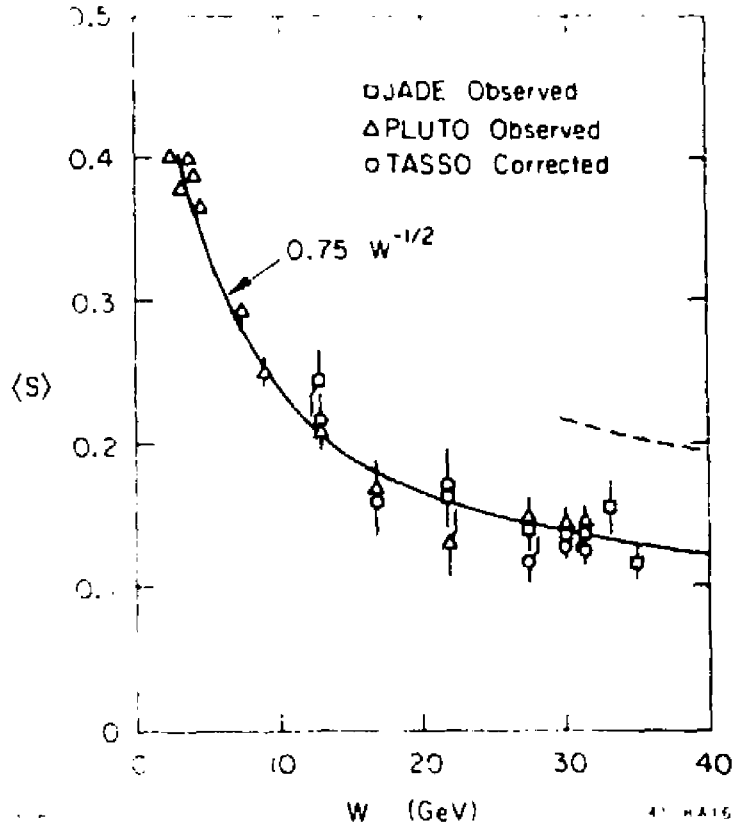
0.5
0.4
0.3
0.2
0.
0
⟨S⟩
□JADE Observed
△PLUTO Observed
○TASSO Corrected
0.75 W^-1/2
10
20
30
40
W (GeV)

Fig 29

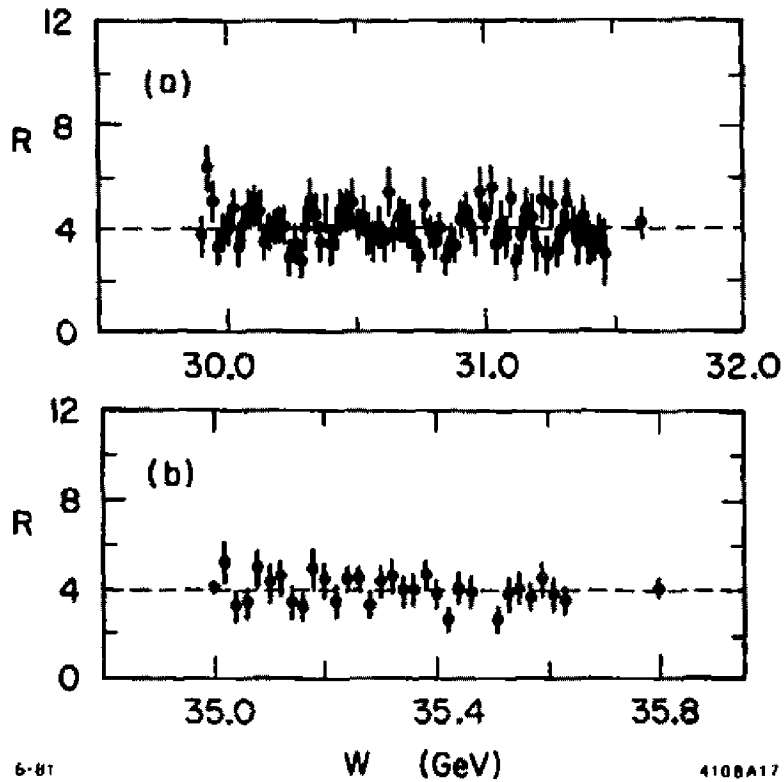

Fig. 30